Review article

Alexander Carmele* and Stephan Reitzenstein

Non-Markovian features in semiconductor quantum optics: quantifying the role of phonons in experiment and theory

Abstract: We discuss phonon-induced non-Markovian and Markovian features in QD-based quantum nanooptics. We cover lineshapes in linear absorption experiments, phonon-induced incoherence in the Heitler regime, and memory correlations in two-photon coherences. To qualitatively and quantitatively understand the underlying physics, we present several theoretical models that capture the non-Markovian properties of the electron–phonon interaction accurately in different regimes. Examples are the Heisenberg equation of motion approach, the polaron master equation, and Liouville propagator techniques in the independent boson limit and beyond via the path integral method. Phenomenological modeling overestimates typically the dephasing due to the finite memory kernel of phonons and we give instructive examples of phonon-mediated coherence such as phonon-dressed anticrossings in Mollow physics, robust quantum state preparation, cavity feeding, and the stabilization of the collapse and revival phenomenon in the strong coupling limit of cavity quantum electrodynamics.

Keywords: phonons; semiconductor quantum dots; open quantum system; quantum optics.

1 Introduction

Since the seminal demonstration of optically [1] and electrically triggered [2] single-photon emission, deterministic generation of entangled photon pairs [3, 4], near-unity indistinguishable photons [5], and strong coupling to a microcavity [6] with semiconductor quantum dots (QDs) [7, 8], acting as active quantum light emitters, there has been a steadily increasing number of research activities to establish semiconductor systems, in particular QDs, as a key element for modern photonic quantum technologies [9–19]. Focusing on the goal to implement QDs in quantum sensing, metrology, and quantum cryptography and to establish them as "artificial atoms" and ideal candidates for solid-state quantum bits (qubits) and scalable quantum information processing [13, 20–22], it has become clear that QDs cannot be considered as isolated quantum emitters but interact intrinsically with their semiconductor bulk environment. This coupling has usually detrimental impact as it leads to decoherence of the confined exciton acting via superposition states as a qubit [23, 24]. Interestingly, it can also be of positive impact and facilitate, for instance, attractive phonon-mediated resonant excitation schemes [25–27] or phonon-induced quantum coherences [28, 29].

A major phonon coupling mechanism stems from the surrounding host material and its lattice vibrations [8, 30, 31]. The associate distortion of the underlying crystal structure leads inevitably to electron–phonon interaction and subsequently to substantial new forms of decoherence unknown in standard atom–molecular optics (AMO). Because the phonon reservoir is structured, that is, the coupling is frequency-dependent, the influence of phonons on the quantum optical properties of QDs is of non-Markovian nature [23, 32–34]. Thus, to quantify and unravel the underlying physics, non-Markovian dissipative processes need to be taken into account. However, non-Markovianity refuses a time-local formulation, and therefore typical quantum dissipative treatments become unavailable [35, 36] and advanced, or perturbative methods need to be employed [37–41].

Before we discuss the electron–phonon interaction in more detail, we want to briefly comment on how the term "non-Markovian" and "Markovian" is used in this

*Corresponding author: Alexander Carmele, Technische Universität Berlin, Institut für Theoretische Physik, Nichtlineare Optik und Quantenelektronik, Hardenbergstraße 36, 10623 Berlin, Germany, e-mail: alex@itp.tu-berlin.de. https://orcid.org/0000-0001-8108-2973
Stephan Reitzenstein: Technische Universität Berlin, Institut für Festkörperphysik, Optoelektronik und Quantenbauelemente, Hardenbergstraße 36, 10623 Berlin, Germany

review. We adapt the definition of Markovian and non-Markovian processes as formulated among others in Refs. [37, 41]. A system–reservoir interaction is Markovian if the reservoir correlation time vanishes or can be assumed to be negligible for the given set of observables of interest. For example, the correlation function of a reservoir consisting of harmonic oscillators with annihilation (creation) operators $b_{\mathbf{q}}^{(\dagger)}$ with bosonic commutation relation $[b_{\mathbf{q}}, b_{\mathbf{q}'}^{\dagger}] = \delta(\mathbf{q} - \mathbf{q}')$ can be written as:

$$\langle R(t)R(t')\rangle = \sum_{\mathbf{q},\mathbf{q}'} g_{\mathbf{q}}^* g_{\mathbf{q}'} [e^{-i\omega_q t + i\omega_{q'} t'} \langle b_{\mathbf{q}} b_{\mathbf{q}'}^{\dagger}\rangle + e^{i\omega_q t - i\omega_{q'} t'} \langle b_{\mathbf{q}}^{\dagger} b_{\mathbf{q}'}\rangle]$$
$$= \sum_{\mathbf{q}} |g_{\mathbf{q}}|^2 [(2n_q + 1)\cos[\omega_q(t-t')] - i\sin[\omega_q(t-t')]]$$

(1)

where $R(t) = \sum_{\mathbf{q}} g_{\mathbf{q}}(b_{\mathbf{q}} \exp[-i\omega_q t] + b_{\mathbf{q}}^{\dagger} \exp[i\omega_q t])$ and an initial thermal equilibrium at $1/\beta = k_B T$ has been assumed with $\langle b_{\mathbf{q}}^{\dagger} b_{\mathbf{q}}\rangle = [\exp(\beta\hbar\omega_q) - 1]^{-1} = n_q$, the Bose–Einstein distribution, and $\langle b_{\mathbf{q}}^{(\dagger)} b_{\mathbf{q}}^{(\dagger)}\rangle = 0$. If now the relaxation time of the reservoir is much smaller than the evolution time of the observed system, that is, $\mathrm{Re}[\langle R(t)R(t')\rangle] = \Gamma\delta(t-t')$, the system's evolution does not depend on former system–reservoir interaction and the process is Markovian [41]. A specific example of a vanishing correlation time is the radiative decay into free space, where the vacuum field amplitude is nearly constant in the regime of optical system–reservoir interaction and justifies within the small-bandwidth assumption a Lindblad formulation of the process as shown in standard quantum optics books [35–38]. In this case, the dissipative processes can be included via time-independent Lindblad superoperators [35].

A standard example for non-Markovian processes is the electron–phonon interaction in semiconductors [7, 23, 24, 42], where the timescale of the interaction is in the same regime as the corresponding mode structure (ps), and the environment correlation time is finite. In this case, a backflow of information between environment and system takes place and leads to non-Lorentzian lineshapes (e.g. [43]), longer Wigner delay times [44], reappearance of Rabi oscilllations (e.g. [33, 45]), or allows for robust state preparation protocols (e.g. [25, 27, 46–48]), phonon-mediated quantum coherences (e.g. [28, 29, 49]), and incoherent excitation processes such as cavity feeding (e.g. [50, 51]), pulse area–dependent damping, renormalization of Rabi oscillations [23, 45], and excitation-induced dephasing of Mollow triplet sidebands [52–54] as will be discussed in detail below. Thus, when we refer to non-Markovian processes, we mean in general a process that cannot be described with a time-independent, global, Lindblad-based master equation as the paradigm for delta-correlated white noise [35–38, 55].

In the following, we review exemplarily recent work on non-Markovian and Markovian signatures of electron–phonon dynamics in semiconductor QDs [7, 42]. In particular, we focus on most mature InGaAs/GaAs QDs (QDs) with dominant coupling to longitudinal acoustic (LA) and longitudinal optical phonons (LO) via the deformation or respective Fröhlich coupling element [24]. For detailed discussion of semiconductor nanostructures, and the effort of microscopical calculations to quantify coupling mechanism in semiconductors, we refer to relevant books [8, 56] and reviews [57–60].

For the sake of compactness, we do also not include explicitly results in the research efforts of higher-dimensional semiconductor nanostructures such as quantum wires, quantum wells, or mesoscopic bulk systems [61, 62]. There is a wide range of exciting phenomena in these systems because of the ubiquitous non-Markovian electron–phonon and electron–electron dynamics. To name a few, quantum wires show phonon-enabled thermal conductivity [63] based on a universal quantum of thermal conductance [64]. Pronounced non-Markovian decoherence is demonstrated in localized nanotube excitons [32], and also phonon-assisted Anderson localization phenomena have been investigated [65]. In quantum wells, coherent acoustic oscillations are studied [66], and nonequilibrium cooling effects bottlenecked by non-Markovian phonon dynamics have been discussed [67]. Four-wave mixing techniques allow to study and characterize giant excitonic resonances [68, 69], and via two-dimensional coherent spectroscopy techniques, incoherent exciton–phonon Green's function can be probed and extracted in disordered quantum wells [70, 71].

Moreover, optical and electronic two-dimensional spectroscopy has drawn a lot interest recently, as non-Markovian, anomalous lineshapes and relaxation/scattering processes can be characterized and studied in depth. For example, the study of signatures of spatially correlated noise and nonsecular effects [72] has been performed, the read-out of Rabi oscillations in QDs [73], exciton coherence at room temperature [74] investigated, systematic study of dephasing processes including quadratic electron–phonon coupling for elevated temperatures [75, 76] and phonon sidebands in transition metal dichalcogenides have furthermore been demonstrated [77]. Despite the exciting results in higher-dimensional nanostructures and two-dimensional coherent spectroscopy, we focus in the following on a single material platform, semiconductor QDs. This allows us to discuss in detail instructive experimental examples in which the phonon interaction is the dominant source of decoherence and theoretical models, which are capable to capture their specific details

and can partially be treated even analytically. These models are, however, not limited to the QD case and are used for other material platforms such as quantum wells, quantum wires, or atomic-thin two-dimensional systems as well [61, 78, 79].

2 Structure of the review and Hamiltonians

This review covers two different interaction schemes, electron–light ($e - l$) and electron–phonon ($e - p$) dynamics, and is basically structured by increasing complexity. To increase readability, we introduce here the corresponding Hamiltonians, which are used throughout the review. The electron–light interaction is treated either semiclassically H_{e-l}^{sc}, quantized in a mode continuum H_{e-l}^{con}, or within a cavity or single mode description H_{e-l}^{cav}. The Hamiltonians read:

$$H_{e-l}^{sc} = \hbar\Delta\sigma_{22} + \hbar\Omega(t)(\sigma_{21} + \sigma_{12}),$$ (2)

$$H_{e-l}^{cav} = \hbar\omega_{21}\sigma_{22} + \hbar\omega_0 c^\dagger c + \hbar g(c^\dagger\sigma_{12} + \sigma_{21}c)$$ (3)

$$H_{e-l}^{con} = \hbar\omega_{21}\sigma_{22} + \hbar\int d\omega(\omega\, c_\omega^\dagger c_\omega + g c_\omega^\dagger\sigma_{12} + g\sigma_{21}c_\omega),$$ (4)

where the rotating-wave approximation has been applied, and $\Omega(t)$ is the Rabi frequency, including the external driving field $E(t)$ with frequency ω_L and the dipole moment of the QD $\mathbf{d}_{12} = \mathbf{d}_{21}$, assumed in the following as real number, between the conduction 2 and valence band 1 with a bandgap energy of $\hbar\omega_{21}$. In the semiclassical case (H_{e-l}^{sc}), the Hamiltonian is written in the rotating frame of the laser frequency, leading to a detuning of $\Delta = \omega_{21} - \omega_L$. The operator σ_{ij} flips the state $|j\rangle$ to $|i\rangle$, whereas $c^{(\dagger)}$, $c_\omega^{(\dagger)}$ annihilates (creates) a photon in the corresponding mode with bosonic commutation relation $[c_\omega, c_{\omega'}^\dagger] = \delta(\omega - \omega')$. The interaction strength between photons and electron is denoted g, assuming a Wigner–Weisskopf-like coupling with an approximate constant vacuum field amplitude [35, 36].

The second interaction we consider is the electron–phonon interaction, either in a semiclassical limit H_{e-p}^{sc} or for longitudinal acoustical H_{e-p}^{LA} or longitudinal optical phonons H_{e-p}^{LO}. The Hamiltonians read:

$$H_{e-p}^{sc} = \hbar F(t)\sigma_{22},$$ (5)

$$H_{e-p}^{LA} = \hbar\sum_{\mathbf{q}}\omega_{\mathbf{q}} b_{\mathbf{q}}^\dagger b_{\mathbf{q}} + \hbar\sigma_{22}\sum_{\mathbf{q}} g_{12}^{\mathbf{q}}[b_{\mathbf{q}}^\dagger + b_{\mathbf{q}}],$$ (6)

$$H_{e-p}^{LO} = \hbar\omega_{LO}\sum_{\mathbf{q}} b_{\mathbf{q}}^\dagger b_{\mathbf{q}} + \hbar\sigma_{22}\sum_{\mathbf{q}} f_{12}^{\mathbf{q}}[b_{\mathbf{q}}^\dagger + b_{\mathbf{q}}],$$ (7)

where $F(t)$ denotes a stochastic force acting on the QD, $g_{12}^{\mathbf{q}}$ the electron-longitudinal acoustic, and $f_{12}^{\mathbf{q}}$ the electron-longitudinal optical phonon coupling element. Throughout the review, the standard GaAs phonon bulk parameters are used. For example, in case of an approximative spherical geometry, the acoustical phonon coupling element $g_{12}^{\mathbf{q}} = g_{11}^{\mathbf{q}} - g_{22}^{\mathbf{q}}$ reads, where

$$g_{ii}^{\mathbf{q}} = \sqrt{\frac{\hbar q}{2\rho c_s V}} D_i e^{-\frac{q^2\hbar}{4m_i\omega_i}},$$ (8)

and typical parameters for InGaAs/GaAs QDs are given with sound velocity of GaAs $c_s = 0.00511$ nm/fs, deformation potentials $D_1 = -5.38$ eV, $D_2 = -11.68$ eV, effective masses: $m_2 = 0.063$, $m_1 = 0.45$, confinement energies $\hbar\omega_2 = 0.040$ eV, $\hbar\omega_1 = 0.02$ eV, and mass density of GaAs $\rho = 5370$ kg/m³ [23, 24, 29, 51, 56, 80]. For the longitudinal optical phonons, the Fröhlich coupling applies and reads:

$$f_{ii}^{\mathbf{q}} = -i\sqrt{\frac{e^2\hbar\omega_{LO}}{2V\epsilon_0\epsilon'}}\frac{1}{q} e^{-\frac{q^2\hbar}{4m_i\omega_i}},$$ (9)

with $1/\epsilon' = 1/\epsilon_\infty - 1/\epsilon_s = 0.0119347$ with the static dielectric constant $\epsilon_s = 12.53$ and the high frequency dielectric constant $\epsilon_\infty = 10.9$, and the reciprocal dielectric constant $1/\epsilon_0 = 18.1 e^2/(\text{eV nm})$. The longitudinal optical phonon frequency is in GaAs $\hbar\omega_{LO} = 36.4$ meV.

This review is structured in five parts. After the introduction (Section 1) and this section (Section 2), we discuss nonequilibrium phonon dynamics in the semiclassical regime in Section 3. Here, the light field is treated classically with H_{e-l}^{sc} and acts as an excitation source and a way to probe the system's dynamics. Here, we discuss the electron–phonon and electron–light interaction in different regimes, from weak coupling and weak driving to strong coupling and strong driving, and important theoretical tools are presented and explained in detail.

In Section 4, we include also quantized electron–light interaction in cavity quantum electrodynamics H_{e-l}^{cav} or for a mode continuum H_{e-l}^{con} and show how phonons contribute to quantum optical phenomena, rendering the field of semiconductor quantum optics exciting and novel. This section is structured from the single- and two-photon regime to the many-photon dynamics, including non-Markovian phonons as the main source for decoherence.

We then conclude the review in Section 5 and give a short outlook on future directions. Please refer to the

given Sections for a detailed discussion of the presented material.

3 Nonequilibrium phonon dynamics in semiclassical light–matter interaction

Experimental data on quantum emitters in a solid-state environment, as discussed in the introduction, show the necessity of non-Markovian decoherence models. Modeling the required intrinsic memory of the electron–phonon interaction is theoretically a demanding but also very rewarding task as it provides the link between experimental data and their non-Markovian description. Analyzing decoherence mechanisms in solid-state devices is therefore crucial to understand the underlying physics and to optimize their functionality, in particular when quantum properties are addressed. It is also an important part in the pursuit to realize reliable protocols in future quantum communication networks, which are based on coherent light–matter interfaces and the exchange of quantum information via single photons and entangled photon pairs with high indistinguishability [81, 82]. Here, light–matter interaction between two-level emitters and the coherent light fields of an external laser is a well-established approach to investigate the time evolution of the polarization density within a medium [83, 84]. This time evolution can be governed by semiclassical, Maxwell type of dynamics, or takes place deep in the quantum regime of single-emitter–light interaction. However, in this section, we discuss nonequilibrium phonon dynamics in the semiclassical regime.

The achievements in fabrication of high-quality QDs acting as close-to-ideal two-level emitters in the solid state [22, 85] established the possibility to investigate the light–matter interaction in different regimes. This section is structured from the weak electron–phonon coupling and weak driving limit (linear) to the strong electron–phonon coupling and strong driving regime (Mollow regime).

We start in Section 3.1 with the discussion of the impact of lattice distortion processes in absorption experiments [24, 83, 86]. In this linear regime, the QD emission can be expressed via the absorption coefficient $\alpha(\omega)$ and calculated exactly via the independent boson model [37, 87]. Phonon-induced non-Lorentzian lineshapes are unraveled in the absorption coefficient, and a clear deviation from Gaussian white noise correlation is observed

and successfully explained with wavefunctions based on 8 band $\mathbf{k} \cdot \mathbf{p}$ theory and with inclusion of non-Markovian phonon effects [43].

We continue in Section 3.2 with the weak driving or Heitler regime in which we investigate the emission and scattering of a single QD under pulsed excitation [44]. This regime allows us to explore an intriguing quantum optical effect namely the Wigner time delay known from atomic physics [88–90]. This delay originates form the phase shift between the exciting and emitted field because of the finite dwelling time of the excitation in the QD before the QD relaxes. Phonon-induced incoherent processes explain maximal achievable Wigner delay times $\tau_w(\Delta)$ in the nontrivial detuning dependence between the laser and the QD transition [44], which cannot be described by conventional optical Bloch equations [89]. Here, we discuss semiconductor Bloch equations with phonon contributions via the cluster expansion approach [79, 91], which allows perturbatively to take into account nonequilibrium and non-Markovian phonon dynamics. We also show that for low temperatures and weak electron–phonon coupling, the perturbative cluster expansion solution agrees well with the solution from the exact independent boson model, given in Section 3.1.

In the weak electron–phonon coupling but strong driving limit (Section 3.3), non-Markovian features are also captured in the perturbative cluster expansion approach [23, 79, 92–95]. In this limit, ultralong dephasing times can be explained [31] and the recurrence of Rabi oscillations for large pulse areas [23, 33, 46] is seen. This method allows a fast and good approximation to quantify influences of the microscopic properties of the nanostructure under investigation [78, 96]. As an example for signatures typically not present in Lindblad (Markovian) master equation simulations, we present in detail damped Rabi oscillations via longitudinal acoustic phonons. Within the same theoretical framework but in fourth-order perturbation theory, phonon-assisted state preparation protocols are discussed. Those protocols are robust against the underlying geometry of the nanostructure; however, the wavefront of the outgoing acoustic excitations differs strongly for different geometries [27, 46, 96].

Beyond the weak electron–phonon coupling but still in the perturbative regime (Section 3.4), master equation approaches within a dressed-state basis are typically used [35, 37, 97]. We first discuss the Markovian limit [98–101] in Section 3.4 and give an analytical solution for the power spectrum of a resonantly and optically driven QD subjected to Markovian pure dephasing [102]. The Markovian limit, however, cannot capture incoherent excitation processes via phonon feeding [50]. To model such processes

correctly, a Polaron master equation is a feasible model to include as much information as possible from the non-equilibrium phonon dynamics in second-order perturbation theory [51, 97, 103, 104] and shows already very good agreement with experimental data [50]. We derive the polaron master equation explicitly and show that for the weak coupling limit in secular approximation, the cluster expansion solution and polaron master equation dynamics agree well as long as the exciting laser field amplitude is time-independent.

We conclude this section with exact solutions of the electron–phonon interaction. In case of a dispersionless phonon mode, such as longitudinal optical (LO) phonons in the Einstein approximation, an inductive equation of motion scheme leads to numerically exact solutions, cf. Section 3.5. As an example, we show phonon-assisted anticrossings in the Mollow regime, which give experimental access to the Huang-Rhys factor. This shows that the equation of motion approach based on the semiconductor Bloch equations [61, 79, 91] is not limited to the weak coupling regime in principle. If the dispersion relation is nearly constant, as for LO phonons, an inductive equation of motion approach can be used to take into account higher-order phonon processes [28, 105, 106]. In this case, the equation of motion approach becomes a numerically exact method and allows to compute LO phonon–assisted Mollow triplet spectra. Because of the strong driving limit, anticrossings between polaronic and polaritonic dressed states occur and the electron–LO phonon coupling strength can be spectrally obtained because of the emerging splitting [107]. In case of linear, or nonconstant dispersion, this method also still possible to employ is numerically very expensive and therefore not feasible anymore.

In the limit of time-dependent pulses and/or strong coupling to phonons with nonconstant dispersion relation (Section 3.6), perturbative approaches and master equation models do not capture the phonon-induced dynamics accurately anymore [108]. Given the non-Markovian and therefore entangled system–bath dynamics, density matrix renormalization group techniques [109, 110] or exact diagonalization become the only choice. They allow for numerical expensive but exact treatments. Examples are matrix product state evolution techniques [111–114] or the real-time path integral method [33, 115] in which the time evolution is discretized and the dissipative quantum kinetics becomes solvable because of the finite memory of the dissipative kernel, here of the acoustic phonons. Within the path integral method technique, excellent agreement between theory and experiment has been demonstrated for state preparation protocols [25] and

the description of phonon-induced dephasing of coupled QD microcavity systems in the strong coupling regime of cavity quantum electrodynamics [116, 117].

3.1 Non-Lorentzian lineshapes (independent boson model)

For weak coherent pumping, a system is well described in the linear response regime [83]. Via a probe field, the absorption of the nanostructure, here, for example, an ensemble of QDs is quantified via the Beer–Lambert law [118]. The absorption coefficient reveals resonances of the emitter sample, but, more importantly, the interaction with the environment is probed also via the detuning dependence of the absorption. The corresponding lineshape gives access to important information about the kind of coupling (e.g. Fröhlich, deformation, or piezoelectric interaction between electrons and phonons) and the linewidth allows one to conclude about the effective electron–phonon coupling strength [7, 8, 12, 56]. A characteristic quantity to connect theory to experiment is the absorption coefficient, which can be expressed via the susceptibility $\alpha(r, \omega) = \mathrm{Im}[\chi(r, \omega)]$.

In the semiclassical description, we assume an incoming electromagnetic field $\mathbf{E}(r, t)$ described via Maxwell's equations including material contributions. The dynamics of the electric component is described via the homogeneous equation: $\nabla \times \mathbf{E} = -\partial_t \mathbf{B}$, and the inhomogeneous $\nabla \times \mathbf{B} = \mu_0 \mathbf{j} + \partial_t \mathbf{E}/c^2$ with the speed of light in the vacuum $c_0 = (\epsilon_0 \mu_0)^{-1/2}$. Averaging over microscopic degrees of freedom below the optical wavelengths, assuming an electrically neutral sample without a macroscopic current, and neglecting magnetic contributions, we yield for the averaged current: $\mathbf{j}(r, t) \equiv \partial_t \mathbf{P}(r, t)$ [78, 83, 118]. Deriving the wave equation in frequency domain for the electric field, we obtain:

$$\left[\Delta + \frac{\omega^2}{c_0^2} \right] \mathbf{E}(r, \omega) = -\mu_0 \omega^2 \mathbf{P}(r, \omega), \qquad (10)$$

where we assume a purely transversal wave and we neglect in the following out of notation convenience the background material refractive index. If the sample is isotropic, homogeneous, and linear, the polarization is related to the electric field: $\mathbf{P}(r, \omega) = \epsilon_0 \chi(r, \omega) \mathbf{E}(r, \omega)$ and we derive the solution of the field intensity (propagating in z-direction):

$$\begin{aligned} I(z, \omega) = |\mathbf{E}(r, \omega)|^2 = |E_0|^2 \exp[i(k - k^*)z] \\ = |E_0|^2 \exp[-2\mathrm{Im}[k]z], \qquad (11) \end{aligned}$$

with $k = k_0\sqrt{n(r, \omega)}$, the refraction index of the investigated sample $n(r, \omega) = \sqrt{1 + \chi(r, \omega)}$ and $k_0 = \omega/c_0$. The imaginary part of the wave number is directly proportional to the imaginary part of the susceptibility. The susceptibility in the linear regime is connected to the dipole density, which is microscopically given via the transition amplitudes multiplied by their dipole momentum and the average dipole density in the sample with emitter density n_0:

$$\mathbf{P}(r, \omega) = n_0 \sum_{ij} \mathbf{d}_{ij}(r)\rho_{ij}(\omega) \qquad (12)$$

with $\rho_{ij}(t) = \langle i|\rho(t)|j\rangle$. Therefore, the density matrix equation gives access to the linear and, also, nonlinear response of the system via solving the Liouville–von Neumann equation $i\hbar\dot{\rho}(t) = [H, \rho]$.

In the following, a sample consisting of QDs in the two-level approximation is assumed, which is probed via an incoming (linear polarized) field with an amplitude parallel to the dipole moment of the two-level emitters [119]. The associated Hamiltonian H_{e-l}^{sc} is given in Eq. (2). The noncoherent contributions are considered by the decoherence inducing Hamiltonian $H_{e-p}^{st}(t)$ given in Eq. (5) with a c-valued stochastic force F(t). The dynamics of the transition amplitudes reads in general:

$$\partial_t \rho_{12} = i\Delta\rho_{12} - i\Omega(t)\rho_{22} + i\Omega(t)\rho_{11} - \frac{i}{\hbar}\langle 1|[H_{e-l}^{st}(t), \rho(t)]|2\rangle. \quad (13)$$

In the linear regime (no population change is induced), we set $\rho_{11}(t) \approx \rho_{11}(0) = 1$ and a time-independent weak driving field $\Omega(t) = \Omega_0$. Using a phenomenological decoherence model, we choose a stochastic force contribution to the energy splitting between ground $|1\rangle$ and excited state $|2\rangle$, that is, $\omega_{21} + F(t)$ [38, 120]. The formal solution of the transition dynamics in the linear regime reads then with $\xi(t) = \int_0^t dt' F(t')$:

$$\rho_{12}(t) = e^{i\Delta t + i\xi(t)}\left(\rho_{12}(0) - i\Omega_0\rho_{11}(0)\int_0^t dt' e^{-i\Delta t' - i\xi(t')}\right). \quad (14)$$

Because of the decoherence-inducing contributions $\xi(t)$, the equation must be averaged [120]. Assuming the white noise limit, we average with a Gaussian probability distribution, taking only two-body correlations into account [120]. In this limit, we characterize the correlation function as $\langle\langle F(t)F(t')\rangle\rangle = 2\gamma\delta(t-t')$ with $\langle\langle F(t)\rangle\rangle = 0$ and obtain $\langle\langle e^{\pm i\xi(t')}\rangle\rangle = \exp[-\gamma t]$. Given the dephasing, the solution of the transition dynamics is obtained after a simple integration:

$$\langle\langle\rho_{12}(t)\rangle\rangle = e^{i\Delta t - \gamma t}\left(\rho_{12}(0) - i\Omega_0\rho_{11}(0)\frac{e^{-i\Delta t + \gamma t} - 1}{-i\Delta + \gamma}\right). \quad (15)$$

Differentiating with respect to time and taking the Fourier transform into account, we find an expression for the polarization density in the linear regime, projected along the direction of the dipole:

$$\begin{aligned} P(r, \omega) &= n_0 d_{12}[\langle\langle\rho_{12}(\omega)\rangle\rangle + \langle\langle\rho_{21}(\omega)\rangle\rangle] \\ &= n_0 d_{12}\left[\frac{\Omega_0\rho_{11}(0)}{\omega - \Delta - i\gamma} - \frac{\Omega_0\rho_{11}(0)}{\omega + \Delta - i\gamma}\right]. \end{aligned} \quad (16)$$

We have already assumed a linearly polarized electrical field with a real amplitude parallel to the dipole: $\Omega_0 = d_{21}E_0/\hbar$. Ignoring the off-resonant parts of the susceptibility, we find with $\rho_{11}(0) = 1$:

$$\chi(r, \omega) = \frac{n_0|d_{12}|^2}{\epsilon_0\hbar}\frac{i\gamma}{(\omega - \omega_{21})^2 + \gamma^2}, \quad (17)$$

which connects to the absorption of the incoming electric field via the Beer–Lambert law: $I(z, \omega) = |E_0|^2 \exp(-2\text{Im}[\chi]z)$. The higher the dipole density, the larger the individual dipole moments and closer the incoming wave is resonant with the transitions, the stronger is the absorption of the incoming wave into the sample.

The aforementioned absorptive behavior is experimentally accessible via luminescence signals. In the limit of Fermi's golden rule and after subtracting a constant offset, the absorption is proportional to the luminescence signal. This assumption is valid up to second order in the time-evolution operator and within the classical Condon approximation for semiclassical light–matter interaction [83]. These requirements are nevertheless fulfilled in most of the cases, and absorption and luminescence lineshapes are mirror images of each other. In the phenomenological model discussed above, a Lorentzian lineshape is obtained, cf. Eq. (16). However, comparing the experimental luminescence signal of a single QD nonresonantly driven via current injection in the p-i-n diode structure, cf. Figure 1A and B, strong deviations from a Lorentzian oscillator model are visible. The line broadening has a temperature-dependent shoulder, which cannot be explained with a white noise model as outlined above. In contrast, the asymmetric lineshape is a direct consequence of the underlying non-Markovian dynamics between the QD and lattice vibrations [24, 30, 73, 76, 93, 121, 122].

To model the microscopic interaction between the weakly driven QD and its semiconductor host matrix more accurately, we choose the quantized electron–phonon Hamiltonian $H_{e-p}^{la}(t)$ given in Eq. (6) already in the interaction picture with the free evolution governed by $H_p = \hbar\sum_q \omega_q b_q^\dagger b_q$ [24, 93, 123]. To solve the quantum mechanical decoherence model, we have to take into
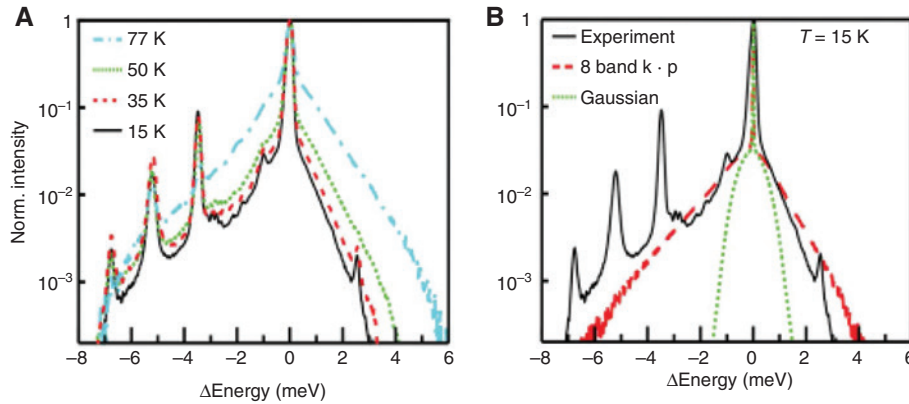
Figure 1: Semilogarithmic plot of the electroluminescence intensity of a single QD.
(A) With increasing temperature the line broadening increases due to stronger acoustic phonon interaction. (B) Comparison of the measured lineshape with two calculated spectra, using alternatively a simple Gaussian (green dotted curve) or a realistic 8 band $\mathbf{k} \cdot \mathbf{p}$ wave function (red dashed curve). Reprinted figure with permission from [43]. © 2011 by the American Physical Society.

account the quantum mechanical character of the decoherence Hamiltonian. The full solution of the density matrix evolution reads in the Liouville space:

$$\rho(t) = T\left\{ \exp\left[\int_0^t L(t_1) dt_1 \right] \rho(0) \right\} \qquad (18)$$

with time-ordering operator T and Liouvillean superoperator $L(t)\rho = (-i/\hbar)[H(t), \rho]$. To derive the systems dynamics, we trace out the phonon degrees of freedom:

$$\mathrm{Tr}_B\{\rho(t)\} = \rho_s(t) = T_s\left\{ \mathrm{Tr}_B\left\{ T \exp\left[\int_0^t L(t_1) dt_1 \right] \rho(0) \right\} \right\}, \qquad (19)$$

where the time-ordering operators ensure that the corresponding von-Neumann equation is still solved. To evaluate this solution, typically a path integral method is used, cf. Section 3.6. Here, we assume a vanishing light–matter coupling and stay in the linear regime. In this case, Eq. (19) can be solved analytically for $H(t) = H_{e-p}^{LA}(t)$ [24, 37, 124].

To solve the quantum mechanical model in the linear regime, one traces out first the electronic degrees of freedom:

$$\frac{d}{dt}\langle 2 | \rho(t) | 1 \rangle = -i\langle 2 | [H_{e-p}^{LA}(t), \rho(t)] | 1 \rangle$$
$$= -i\sum_{\mathbf{q}} g_{12}^{\mathbf{q}}\left[b_{\mathbf{q}}^\dagger(t) + b_{\mathbf{q}}(t) \right]\langle 2 | \rho(t) | 1 \rangle. \qquad (20)$$

This equation can be formally solved via the Dyson series with $\langle 2 | \rho(t) | 1 \rangle = P_B(t)$:

$$P_B(t) = T\left\{ \exp\left[-i\int_0^t dt_1 H_{e-p}^{LA}(t_1)/\hbar \right] P(0) \right\}$$

Assuming discrete time steps Δt, we can write

$$P_B(N\Delta t) = T\left\{ \exp\left[-i\sum_{n=1}^N H_n \right] P(0) \right\}$$
$$= \exp[-iH_N] \cdots \exp[-iH_2] \exp[-iH_1] P(0) \qquad (21)$$

after performing a Suzuki–Trotter decomposition and using the abbreviation

$$H_N := \int_{(N-1)\Delta t}^{N\Delta t} dt \, H_{e-p}^{LA}(t)/\hbar. \qquad (22)$$

The time-order is now trivially fulfilled and therefore, the time-ordering operator is omitted. The necessary condition for the analytical solution in this case is that the commutator of two Hamiltonians is a c-value and not an operator anymore:

$$[H_N, H_{N-1}] = -2i\int_{(N-1)\Delta t}^{N\Delta t} dt_1 \int_{(N-2)\Delta t}^{(N-1)\Delta t} dt_2 \sum_{\mathbf{q}} |g_{12}^{\mathbf{q}}|^2 \sin[\omega_q(t_1 - t_2)]. \qquad (23)$$

This result means that the commutator of the individual Hamiltonian with the commutator of the Hamiltonians vanishes $[[H_i + H_j], [H_i, H_j]] = 0$, and therefore the Baker–Campbell–Hausdorff formula can be used $\exp[A]\exp[B] = \exp[A + B]\exp[[A, B]/2]$ to obtain in the limit of $\Delta t \to 0$:

$$P_B(t) = \exp\left[-i\int_0^t dt_1 H_{e-p}^{LA}(t_1)/\hbar \right] P(0)$$
$$\exp\left[\frac{1}{2\hbar^2} \int_0^t dt_1 \int_0^{t_1} dt_2 [H_{e-p}^{LA}(t_1), H_{e-p}^{LA}(t_2)] \right]. \qquad (24)$$

Because the time-ordering has been taken into account already, one can trace out the phonons and the independent boson model is given via $P(t) := Tr_B[P_B(t)]$

$$P(t) = \exp[i\omega_{21}t + i\text{Im}[\phi_I(t)] - \text{Re}[\phi_I(t)]], \qquad (25)$$

$$\phi_I(t) = \sum_{\mathbf{q}} \frac{|g_{12}^{\mathbf{q}}|^2}{\omega_q^2}[(2n_q + 1)(1 - \cos[\omega_q t]) + i\omega_q t - i\sin(\omega_q t)]. \qquad (26)$$

Obviously, the time-order is fully taken via the imaginary phase whereas the temperature-dependent dephasing stems alone from the part left untouched by the time-ordering. Therefore, neglecting the time-order completely will yield the wrong result interestingly only if phase-dependent quantities are studied.

Taking the Fourier transform, we yield $\rho_{12}(\omega)$ and $\rho_{21}(\omega)$ and the susceptibility includes then non-Markovian effects because of the quantum character of the structured bosonic reservoir. The semiconductor host matrix is considered in the coupling elements, as well as the temperature dependence mainly governed by the phonon frequencies from the dispersion relation, which in principle can be calculated ab initio. In Figure 1B, a microscopic wavefunction is used to model the correct, experimentally observed lineshape [43].

To conclude this section, a non-Markovian dephasing model was applied to describe the emission spectra of a single QD embedded in an electrically pumped device, which is based on a p-i-n diode design and an oxide aperture to spatially restrict the current flow. Despite the complexity of the device design and the electrical excitation scheme, the agreement between the analytical solvable model and experiment is striking. This together with the possibility to include microscopic parameters into the model for the description of experimental results proves the strength of the non-Markovian dephasing model. Noteworthy, the lineshape of the calculated spectra depends only on the electron–phonon coupling matrix elements. Moreover, the sensitivity of the choice of electronic wave function is clearly visible, comparing a Gaussian wave function with an 8 band $\mathbf{k} \cdot \mathbf{p}$ theory [58, 59]. This is an important feature of the advanced model and highlights its usefulness for further optimization and technological fine-tuning of single-QD quantum devices.

3.2 Phonon-enhanced Wigner time delay (Cluster expansion)

Beyond the linear regime but still in the weak excitation limit, the Heitler regime includes nonlinear contributions as it studies the excited state dynamics $\rho_{22}(t) = \langle \sigma_{22}(t) \rangle$ as

a figure of merit in strong contrast to the simpler linear regime, which addresses $\rho_{12}(t) = \langle \sigma_{21}(t) \rangle$. In the Heitler regime, the incoming light is mainly coherently scattered, that is proportional to $|\rho_{12}(t)|^2$, but in dependence on the pulse length and pulse area, a part of the incoming laser excitation is absorbed $\rho_{11}(t) < 1$, converted into electronic excitation $\rho_{22}(t) > 0$ before being emitted back via incoherent scattering. The process of reemission needs a finite time between the incoming pulse and outgoing emission, and the delay between the maximum of the excitation pulse and emission pulse is called Wigner delay or dwell time.

The Wigner delay is ultimately limited by the coherence time $1/T_2 = 1/(2T_1) + 1/T_2^*$ [89] where T_1 denotes the radiative lifetime and T_2^* is the coherence timescale. If no or negligible decoherence is present ($T_2^* \to \infty$) such as in certain atomic systems [88, 90], the maximum Wigner delay reads $2T_1$ as the signal stems from radiative relaxation, and every relaxation induces a partial decoherence between the electronic levels. Because the Wigner delay is limited by the decoherence process in case of solid-state emitters, it is an interesting figure of merit to quantify the effective T_2^* time. In particular when probing the spectral response, the detuning dependence of the Wigner delay reveals clearly a non-Markovian and phonon coupling–dependent feature as we discuss in the following [44].

Because the pulse induces population dynamics of the electronical system, we need to solve the optical Bloch equations. Limiting our analysis of the electronic system to a two-level system, which is in good agreement with the experimental situation of studying InGaAs QD with close to ideal quantum properties at low temperature, we restrict the dynamics first to the Lindblad master equation case with

$$\dot{\rho} = -\frac{i}{\hbar}[H_{e-l}^{sc}(t), \rho] + \frac{\Gamma}{2}\mathcal{D}[\sigma_{12}]\rho + \frac{\gamma_p}{2}\mathcal{D}[\sigma_{22}]\rho, \qquad (27)$$

with $\mathcal{D}[\mathcal{A}]\rho = 2A\rho A^+ - A^+A\rho - \rho A^+A$ as the Lindblad superoperator. Dissipative contributions are taken into account via this Lindblad formalism and can be derived via second-order perturbation theory based on H_{e-p}^{st} for the pure dephasing γ_p and H_{e-l}^{con} for the radiative decay Γ, cf. Section 3.4 for an exemplarily derivation of the pure dephasing Lindblad. The dynamics of the system reads:

$$\dot{\rho}_{22} = -\Gamma\rho_{22} + 2\text{Im}[\Omega(t)\rho_{12}] \qquad (28)$$

$$\dot{\rho}_{12} = (i\Delta - \Gamma/2 - \gamma_p)\rho_{12} - i\Omega(t)(2\rho_{22} - 1), \qquad (29)$$

where we use for the excitation pulse $\Omega(t) = \Omega_L\sqrt{\frac{\pi}{(2\tau^2)}}\exp\left[-\frac{(t - t_0)^2}{2\tau^2}\right]$ with the amplitude Ω_L and

$\Delta = \omega_{21} - \omega_L$. The Heitler regime is given in the low excitation limit, when no Rabi oscillations will be induced and the coherence ρ_{12} is driven weakly and is mainly governed by the detuning and dephasing dynamics $\gamma = \Gamma/2 + \gamma_p$. Therefore, we yield after assuming quasisteady dynamics $(\dot{\rho}_{12} \approx 0)\rho_{12} \approx \Omega(t)(2\rho_{22} - 1)(\Delta - i\gamma)/(\Delta^2 + \gamma^2)$ and the excitation density reads: $2\rho_{22} \approx [1 + (\Delta^2 + \gamma^2)\Gamma/(4\gamma\Omega^2)]^{-1}$. Because the detection is proportional to the coherence time of the electronic signal, the phase shift of the transition dynamics is given in the adiabatic limit. To describe the Wigner time delay in the presence of decoherence, we are not interested in the amplitude but in the phase, which is proportional to $\phi(\omega) = \mathrm{atan}[\Delta/\gamma] + \pi/2$ of the field amplitude $\Delta - i\gamma$. The derivative of the phase with respect to the frequency allows us to find the Wigner delay in the steady-state limit:

$$\tau_W = \frac{d\phi}{d\omega} = \frac{1}{\gamma + \Delta^2/\gamma} \tag{30}$$

which for $\Delta = 0$, $\gamma_p = 0$ yields the maximum of the Wigner delay, namely $\tau_W^{\max} = 2/\Gamma = 2T_1$. However, if we compare the Markovian theory (green and blue lines) with experimental data (black dots) in Figure 2, a Lindblad-based pure dephasing mechanism reproduces either the small or comparably large detuning limit but misses the asymmetry between positive and negative detunings. Importantly, it is not valid in both limits for the same phenomenological γ_p value, whereas the radiative decay Γ and the pulse $\Omega(t)$ are fixed. In contrast to the phenomenological decoherence model,
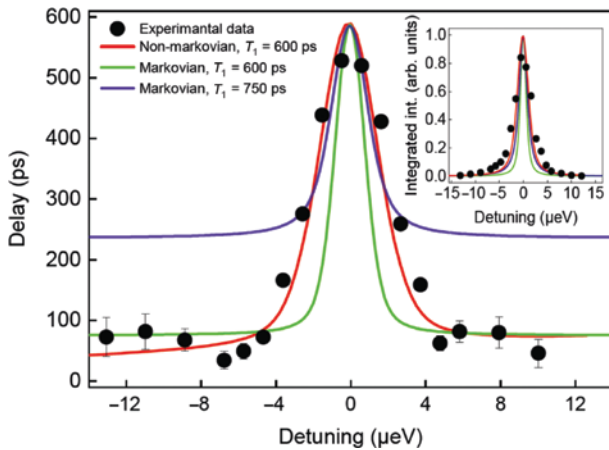

Figure 2: Time delay as a function of spectral detuning between the laser and the TLS.
The red line and black dots correspond, respectively, to the non-Markovian simulations and the experiment as discussed in the main text. Green and blue lines show the simulation obtained via the Markovian approximation. Inset: Integrated intensity of the scattered pulses as a function of detuning. © 2019 American Physical Society, reprinted from [44].

the non-Markovian model, cf. Figure 2 (red line) based on the semiconductor Bloch equation approach reproduces the experimental data for both limits and also exhibits the slight asymmetry between positive and negative detunings with respect to the laser frequency [44]. We will now discuss how to obtain the non-Markovian system response.

In the weak coupling limit, the experimental data are modeled by semiconductor Bloch equations in the Heisenberg picture $-i\hbar \frac{d}{dt}A = [H^{sc}_{e-l} + H^{la}_{e-p}, A]$ from Eq. (2) and (6) with corresponding nonequilibrium phonon contributions [28, 61, 79, 91] and A a quantum mechanical operator such as σ_{22}. In this context, it is important to note that lattice vibrations in semiconductor nanostructures give rise to new effects not encountered in typical atomic quantum optics [125, 126]. These features stem from the non-, that is, sub- or super-Ohmian spectral density of the semiconductor electron–phonon interaction [7, 57, 84, 93]. Corresponding Lindblad-based master equation treatments are derived via Markovian-, Born-, and secular approximation and neglect frequency-dependent system–bath interaction strengths. Furthermore, master equation approaches fail in this case because of the time-dependent pulse, which enforces a time-reordering procedure [127]. Here, we model the dynamics via a Born factorization approach, which is valid up to a temperature of 60 K and in the weak driving limit, cf. Ref. [108], relevant for the description of the data presented in Figure 2.

When solving the semiconductor Bloch equation in the Heisenberg picture, the one-electron assumption is considered $\langle \sigma_{11} \rangle = 1 - \langle \sigma_{22} \rangle$. The phonon dynamics is treated non-Markovianly in the bath assumption limit, that is, second-order Born factorization and the derived set of equations of motion reads (including a Markovian radiative decay constant Γ) with $\langle A(t) \rangle = \mathrm{Tr}[\rho(0)A(t)]$:

$$\frac{d}{dt}\langle \sigma_{22} \rangle = -2\Gamma\langle \sigma_{22} \rangle + 2\mathrm{Im}[\Omega(t)\langle \sigma_{12} \rangle], \tag{31}$$

$$\frac{d}{dt}\langle \sigma_{12} \rangle = -(\Gamma + i\Delta)\langle \sigma_{12} \rangle - i\Omega(t)(2\langle \sigma_{22} \rangle - 1) \\ - i\sum_{\mathbf{q}} g^{\mathbf{q}}_{12}\langle b_{\mathbf{q}}\sigma_{12} \rangle + g^{\mathbf{q}*}_{12}\langle b^{\dagger}_{\mathbf{q}}\sigma_{12} \rangle, \tag{32}$$

$$\frac{d}{dt}\langle b_{\mathbf{q}}\sigma_{12} \rangle = -(\Gamma + i\Delta + i\omega_q)\langle b_{\mathbf{q}}\sigma_{22} \rangle - i\Omega(t)(2\langle b_{\mathbf{q}}\sigma_{22} \rangle \\ - \langle b_{\mathbf{q}} \rangle) - ig^{\mathbf{q}*}_{12}\langle b^{\dagger}_{\mathbf{q}}b_{\mathbf{q}} \rangle\langle \sigma_{12} \rangle, \tag{33}$$

$$\frac{d}{dt}\langle b^{\dagger}_{\mathbf{q}}\sigma_{12} \rangle = -(\Gamma + i\Delta - i\omega_q)\langle b^{\dagger}_{\mathbf{q}}\sigma_{12} \rangle - i\Omega(t)(2\langle b_{\mathbf{q}}\sigma_{22} \rangle^* - \langle b_{\mathbf{q}} \rangle^*) \\ - ig^{\mathbf{q}}_{12}\langle b_{\mathbf{q}}b^{\dagger}_{\mathbf{q}} \rangle\langle \sigma_{12} \rangle, \tag{34}$$

$$\frac{d}{dt}\langle b_{\mathbf{q}}\sigma_{22} \rangle = -(2\Gamma + i\omega_q)\langle b_{\mathbf{q}}\sigma_{22} \rangle - i\Omega(t)(\langle b_{\mathbf{q}}\sigma_{12} \rangle - \langle b^{\dagger}_{\mathbf{q}}\sigma_{12} \rangle^*) \\ + ig^{\mathbf{q}*}_{vc}\langle \sigma_{22} \rangle, \tag{35}$$

$$\frac{\mathrm{d}}{\mathrm{d}t}\langle b_{\mathbf{q}}\rangle = -i\omega_q\langle b_{\mathbf{q}}\rangle - ig_{12}^{\mathbf{q}^*}\langle\sigma_{22}\rangle. \tag{36}$$

The phonon occupation number is given by the Bose–Einstein distribution:

$$\langle b_{\mathbf{q}}^{\dagger}b_{\mathbf{q}}\rangle = [\exp(\hbar\omega_q/(k_BT))-1]^{-1}. \tag{37}$$

Before discussing the Heitler regime, we show the validity of the second-order truncation in the weak coupling limit. In Figure 3, we compare the solution of the independent boson model from Eq. (25) (green) with the perturbative solution in second order (orange) for different temperatures (from top to bottom, 4, 50, 77, 100 K). Assuming an initial delta pulse $\Omega(t)=\delta(t)/2$, the dynamics of the set of equations [Eq. (31–36)] reduces to three equations [Eq. (32–34)] and can also be solved analytically [24, 93]. The resulting dynamics agrees well with the analytically exact solution up to 60 K. If the cluster expansion solution is expanded up to the fourth order, the agreement is even better and holds up to 150 K [108].

Having shown the validity of the perturbative approach, we can discuss the role of phonons in the Heitler regime. In the calculations, the radiative decay time $\Gamma = 650$ ps^{-1} is taken from the experiment, and we choose a phonon coupling strength so that we reproduce the maximum of the Wigner delay on resonance at $\Delta = 0$ for the experimentally given pulse width of $\tau = 1.05$ ns. Via the detuning dependence, the Wigner delay probes the amount of phonon-induced incoherence in the signal

and is a good figure of merit to unravel and to monitor the electron–phonon interaction [50, 107]. Clearly, the non-Markovian theory interpolates between both limits (large and small detuning), cf. Figure 2 (red, solid line), and reproduces also the small temperature-dependent asymmetry because of the preference of the system to emit rather than to absorb phonons at low temperatures. This can be explained with Eq. (33) and (34), as in the low temperature limit mainly $\langle b_{\mathbf{q}}^{\dagger}\sigma_{12}\rangle$ contributes because of spontaneous phonon emission rather than induced absorption and stimulated emission. Because the phonon frequency enters with a different sign into the dynamics of both of the phonon-assisted coherences, the pure dephasing is blue-detuned effectively larger, which leads subsequently to an efficiently larger Wigner delay.

Applying this theory is therefore a key to describe an exciting optical effect known up until now only from atomic physics. Together with experimental data on the Wigner time delay of a single two-level emitter represented by a high-quality QD, it provides important access to the underlying decoherence processes and associated timescales, which will be of importance to tailor such quantum emitters for applications in quantum technology, which requires a high degree of coherence in the generation, transfer, and interfacing of single photons in solid-state quantum devices.

3.3 Phonon-assisted damping of Rabi oscillations and state preparation (cluster expansion)

As have been discussed in the previous section, in the weak coupling regime for the electron–phonon coupling, quantified here via $g_{12}^{\mathbf{q}}$, a factorization approach already mirrors qualitatively and quantitatively the system's dynamics very accurately. A typical factorization approach for time-dependent and time-independent pulses is the Born factorization, typically within the Heisenberg picture of the operator of interest A, for example, $\langle Ab_{\mathbf{q}}^{\dagger}b_{\mathbf{q}}\rangle \approx \langle A\rangle\langle b_{\mathbf{q}}^{\dagger}b_{\mathbf{q}}\rangle$ [37, 38]. To go beyond the Born limit, a systematic correlation expansion approach can be applied [60, 61, 79, 91, 128]. Here, the factorization is accompanied with a correction, and the dynamics of this correction is taken into account up to arbitrary high orders: $\langle Ab_{\mathbf{q}}^{\dagger}b_{\mathbf{q}}\rangle = \langle A\rangle\langle b_{\mathbf{q}}^{\dagger}b_{\mathbf{q}}\rangle + \delta\langle Ab_{\mathbf{q}}^{\dagger}b_{\mathbf{q}}\rangle$ [79, 129]. For the weak coupling limit and nonentangled system reservoir dynamics, this cluster expansion approach gives reliable quantitative agreement for weakly correlated many-body systems [79]. Already on a second-order level, the quantum kinetic dephasing dynamics of optically induced nonlinearities in GaAs QDs can be
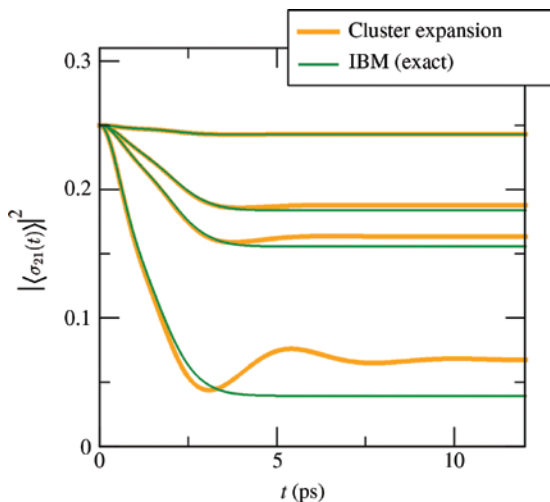
Figure 3: Comparison for different temperatures (from top to bottom 4, 50, 77, 100 K) between the independent boson solution from Eq. (25) (green) and the second-order cluster expansion solution from Eq. (32) with $\Omega(t)=\delta(t)/2$ (orange).
For low temperatures and typical semiconductor parameter as given in the text, the solutions agree well up to around 60 K.

calculated accurately and in agreement with experiments for so far experimentally accessible pulse strengths.

Evaluating the set of equations of motion [Eq. (31–36)] beyond the Heitler regime, Rabi oscillations occur, cf. Figure 4. Here, acoustical phonons renormalize the Rabi energy and result in damping that depends strongly on the input pulse strength, which is not included in a Markovian treatment [23, 130–133]. This can be seen by comparing the dynamics induced by a Markovian, time-independent dephasing (green line) with the non-Markovian, phonon-induced dephasing (orange line) in the excited state density, cf. Figure 4. The Markovian dephasing dynamics overestimates the influence of the phonon strongly and acts continuously with the same damping strength. In contrast, acoustical phonons attack initially the coherences strongly but saturate after few ps, which leads to an almost constant Rabi oscillation amplitude. This shows that Markovian and non-Markovian treatment of decoherence processes lead to qualitative different behavior and are difficult to compare on the same footing. Note also that the results can be obtained in a rate equation approach using corresponding dressed states [134].

Another example is all-optical state preparation [27]. The cluster expansion techniques allows one to investigate the impact of different geometries of the QD in state-preparation protocols. For example, the electron–phonon coupling of a spherical QD and a more realistic lens-shaped QD can explicitly be compared [96]. Interestingly,
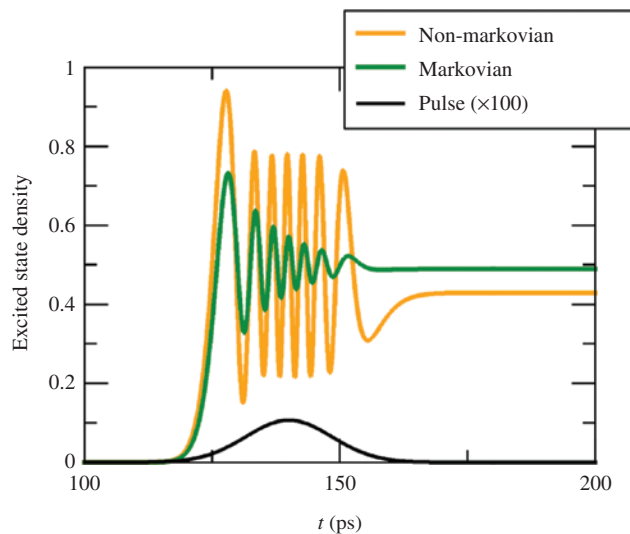
the numerical analysis shows that the QD (electronic) dynamics is hardly influenced on the actual nanostructure geometry, cf. Figure 5D, and depends mainly on the smallest dimension, which governs the electron–phonon interaction. For instance, comparing the state preparation dynamics for different geometries (lens-shaped QD A, spherical B,C with different radii) of the QD's excited state, the qualitative dependence on the pulse area is the same. In this regard, it is noteworthy that the strongly lens-shaped QD A has nearly exact the same pulse area dependence as the spherical QD C despite different spectral densities for the electron–phonon interaction strength. This result allows one to map the electronic dynamics of lens-shaped QDs with spectral densities derived via a spherical geometry when studying the phonon influence on the electronic system. In contrast to the electronic kinetics that are mainly governed by the exciting laser field, the actual nanostructure geometry has a very strong impact on the spatiotemporal properties of the phonon dynamics, cf. Figure 5A and C. An example is given, where for a lens-shaped QD, the phonon emission is strongly concentrated along the direction of the smallest axis of the QD, which
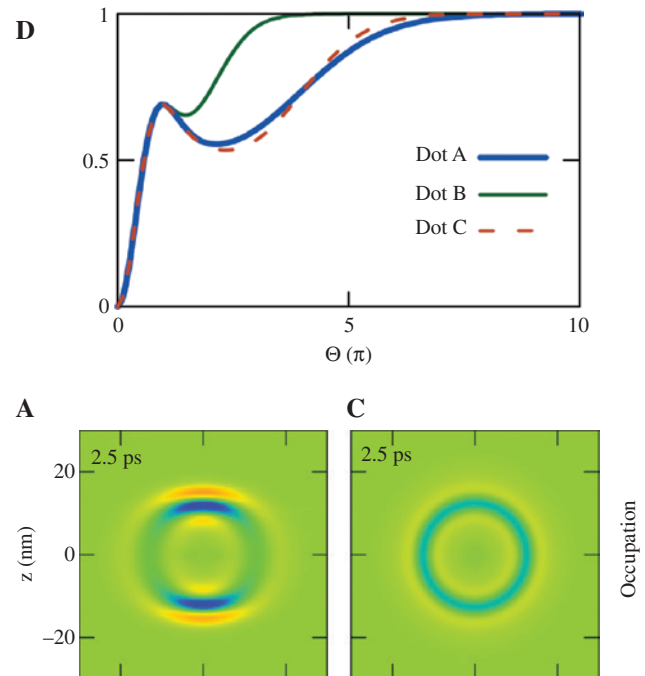

Figure 5: (D) Final occupation of the excited QD state for a strongly lens-shaped QD (A) and two spherical shaped QDs (B, C). Despite different geometries QD, A and C show quantitative and qualitative the same dependence on the pulse area. (A) and (C) The relative volume change after an excitation with a 2π pulse for (A) a lens-shaped and (C) a spherical shaped QD. The outgoing phonon waves differ strongly in directionality. Reprinted figure with permission from [96]. © 2017 by the American Physical Society.

Figure 4: Rabi oscillations of a QD under time-dependent driving (Gaussian pulse, black line).
Non-Markovian electron–phonon interaction (orange line) leads to a renormalization of the Rabi frequency and recovers partial coherence after the first ps in contrast to Markovian damping (green line).

is important for a phonon-mediated coupling of different QD [135, 136]. Therefore, the QD shape plays an important role in determining the properties of the created phonons and possible application for phonon lasing and sensing with solid-state nanostructures [137–139]. Also, it has been shown that adding a high chirp rate to ultrashort laser pulses, the QD can be decoupled from the phononic environment and thus a reappearance of rapid adiabatic passage can be established [46].

3.4 Phonon-assisted incoherent excitation processes (Polaron master equation)

The Heisenberg equation of motion method is in general valid in the weak coupling limit. This is not the case for the strong coupling and high temperature limit, where most perturbative approaches fail. However, in case of a time-independent pump, the Hamiltonian in Eq. (2) can be rewritten in the polaron frame, and a more convenient non-Lindblad type of master equation can be derived [50, 127]. The main goal of the polaron transformation is to trace out the degrees of freedom of the phonon reservoir in a second-order Born theory but to keep as much information as possible about the electron–phonon interaction. In second-order perturbation theory, the reduced density matrix $\text{Tr}_B\{p(t)\} = \rho_s(t)$ in the interaction picture and in second-order Born approximation reads:

$$\dot{\rho}_s(t) = -\frac{i}{\hbar}[H_{e-l}^{sc}, \rho_s(t)] - \frac{i}{\hbar}\text{Tr}_B\{[H_I, \rho_s^I(t) \otimes \rho_B]\} \tag{38}$$

$$-\frac{1}{\hbar^2}\int_0^t d\tau \text{Tr}_B\{[H_I, [H_I(-\tau), \rho_s(t-\tau) \otimes \rho_B]]\}. \tag{39}$$

As a first approach, one can choose a stochastic force via H_{e-p}^{st}. In this case, the interaction Hamiltonian reads $H_I(\tau) = \hbar\sigma_{22}(\tau)F(t+\tau)$ and the trace over the bath degrees of freedom is a Gaussian average $\text{Tr}_B\{\dots \rho_B\} \rightarrow \langle\langle\dots\rangle\rangle$. As the electronic operators are not affected by the statistical average and c-values commute, we obtain:

$$\langle\langle[H_I, [H_I(-\tau), \rho_s(t-\tau)]]\rangle\rangle$$
$$= \hbar^2(\gamma_p/2)\delta(\tau)[\sigma_{22}, [\sigma_{22}(-\tau), \rho_s(t-\tau)]] \tag{40}$$

where we used the white noise correlation for the stochastic force $\langle\langle F(t_1)F(t_2)\rangle\rangle = \gamma_\rho\delta(t_1-t_2)/2$ and $\langle\langle F(t)\rangle\rangle = 0$. In this limit, the master equation reads as given in Eq. (27):

$$\frac{d}{dt}\rho_s(t) = -i[\Delta\sigma_{22} + \Omega(\sigma_{12} + \sigma_{21}), \rho_s(t)]$$
$$+ \gamma_p[\sigma_{22}\rho_s(t)\sigma_{22} - \rho_s(t)]. \tag{41}$$

Such a Markovian limit is valid in many experimental setups and driving scenarios, as long as the dynamics of the chosen observable evolves on a much smaller timescale than the environmental correlation times. For example, Figure 6 depicts excitation-dependent resonance fluorescence emission spectra for different excitation, which were obtained in a unique experiment using a high-β QD microlaser as cw pump [102].

Acting as excitation the electrically driven high-β microlaser drives with its output field, a semiconductor QD. This QD acts as a two-level system within an advanced fiber-coupled experimental setup based on two cryostats, which host the QD microlaser and single QD sample, respectively. The experimental data on the resonantly driven QD are obtained at cyrogenic temperatures of 7 K to minimize electron and hole escape from the QDs and phonon-induced decoherence γ_ρ. However, the emerging Mollow spectra for increasing excitation powers show driving-induced pure dephasing, which we model quantitatively by our model Eq. (41). Indeed, the Markovian
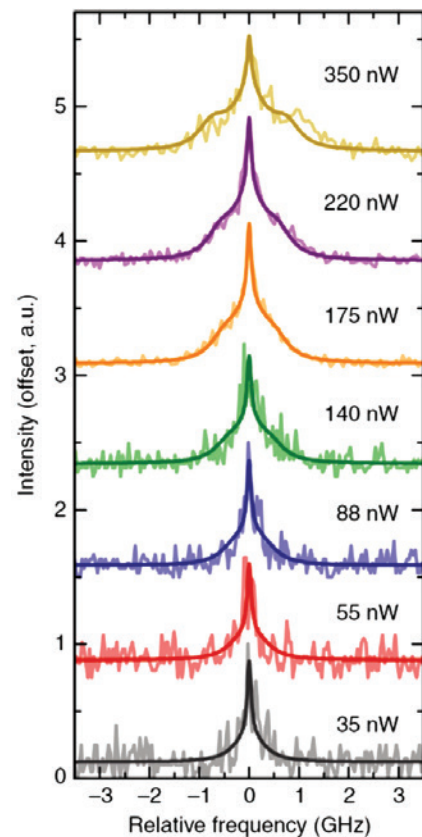

Figure 6: Excitation-dependent resonance fluorescence emission spectra and photon autocorrelation function under cw excitation by a state-of-the-art high-β QD microlaser.
Increasing excitation power leads toward a Mollow-triplet like emission spectrum. Reprinted figure from [102].

theory (solid lines) reproduces well the experimental data for optimum T_2 values around 500 ps. The Mollow spectrum, derived from the power spectrum formula $S(\omega)$, reads:

$$S(\omega) = \lim_{t\to\infty} \text{Re}\left[\int_0^\infty d\tau \langle \sigma_{21}(t)\sigma_{12}(t+\tau)\rangle e^{-i\omega\tau}\right],$$

$$S(\omega) = \frac{\Gamma_R^2}{4\Omega^2 + \Gamma_P\Gamma_R}\pi\delta(\omega-\omega_0) + \frac{\Gamma_P}{(\omega-\omega_0)^2 + \Gamma_P^2}$$
$$+\frac{1}{2}\frac{\Gamma_+ Z_C + (\omega-\omega_0+\Omega_R)Z_S}{\Gamma_+^2 + (\omega-\omega_0+\Omega_R)^2} + \frac{1}{2}\frac{\Gamma_+ Z_C - (\omega-\omega_0-\Omega_R)Z_S}{\Gamma_+^2 + (\omega-\omega_0-\Omega_R)^2},$$

$$(42)$$

where the following abbreviations are used: $\Gamma_R = 2\Gamma$, $\Gamma_P = \Gamma + \gamma_\rho$, and $\Gamma_\pm = (\Gamma_R \pm \Gamma_P)/2$, $\Omega_R = \sqrt{4\Omega^2 - \Gamma_-^2}$ and the oscillator strength functions are introduced:

$$Z_C = 1 - \frac{\Gamma_R^2}{4\Omega^2 + \Gamma_R\Gamma_P} \tag{43}$$

$$Z_S = \frac{\Gamma_R}{\Omega_R}\left(2 - \frac{\Gamma_+}{4\Omega^2 + \Gamma_R\Gamma_P}\right). \tag{44}$$

Although a Markovian model may apply to special situations, more insight into the decoherence processes is feasible to overcome temperature and single-photon repetition rate limitations. As shown above, Markovian, that is, global, frequency-, and time-independent dephasing dynamics do not always model the dynamics correctly, and it is necessary to go beyond the Born–Markovian and secular limit of the master equation.

To include as much information as possible in second-order perturbation theory, we transform the Hamiltonian for a time-independent Rabi frequency $\Omega(t) = \Omega_0$ in Eq. (2) into the polaron frame [51, 97, 103, 104]. We use the electron–phonon interaction Hamiltonian and apply a unitary transform, that is, diagonalization of the phonon part of the Hamiltonian, via $U_p = \exp[\sigma_{22}(R^\dagger - R)]$ and $R = \sum_q g_{12}^q b_q / \omega_q$. The Hamiltonian in the polaron frame can be calculated via $\exp[x]y\exp[-x] = \sum_{n=0}^\infty [x,y]_n/n!$ and $[x,y]_0 = y$, $[x,y]_n = [x,[x,y]_{n-1}]$:

$$U_p\sigma_{22}U_p^\dagger = \sigma_{22}, \tag{45}$$

$$U_p(\sigma_{12}+\sigma_{21})U_p^\dagger = \cosh[R^\dagger - R](\sigma_{12}+\sigma_{21})$$
$$+\sinh[R^\dagger - R](\sigma_{12}-\sigma_{21}), \tag{46}$$

$$U_p b_q^\dagger b_q U_p^\dagger = b_q^\dagger b_q - \sigma_{22}\frac{g_{12}^q}{\omega_q}(b_q^\dagger + b_q) + \sigma_{22}\left(\frac{g_{12}^q}{\omega_q}\right)^2, \tag{47}$$

$$U_p\sigma_{22}(b_q^\dagger + b_q)U_p^\dagger = \sigma_{22}(b_q^\dagger + b_q) - 2\sigma_{22}\frac{g_{12}^q}{\omega_q}. \tag{48}$$

The transformed Hamiltonian is split into an interaction Hamiltonian:

$$H_I/\hbar = (\sigma_{12}+\sigma_{21})(\Omega\cosh[R-R^\dagger]-\bar{\Omega})$$
$$+\Omega(\sigma_{21}-\sigma_{12})\sinh[R-R^\dagger], \tag{49}$$

with $\bar{\Omega} = \Omega\langle\exp[R^\dagger - R]\rangle = \Omega\exp[-\phi(0)/2]$ where $\phi(t)$ denotes the phonon correlation of the diagonalized electron–phonon interaction:

$$\phi(t) = \sum_q |g_{12}^q/\omega_q|^2\left(\coth\left[\frac{\hbar\omega_q}{2k_bT}\right]\cos(\omega_q t) - i\sin(\omega_q t)\right). \tag{50}$$

The corresponding Hamiltonian of the free evolution reads:

$$H_0/\hbar = \Delta\sigma_{22} + \bar{\Omega}(\sigma_{12}+\sigma_{21}) + \sum_q \omega_q b_q^\dagger b_q, \tag{51}$$

with $\Delta = \omega_{21} - \omega_L - \sum_q \frac{|g_{12}^q|^2}{\omega_q}$. Additionally the Franck–Condon renormalization $\bar{\Omega}(\sigma_{12}+\sigma_{12})$ is introduced to the free evolution and subtracted from the interaction Hamiltonian to ensure in second-order perturbation theory in $H_I(t)$ a vanishing first-order contribution: $\text{Tr}\{[H_I(t), \rho_s^I(t)\otimes\rho_B]\} = 0$, and the resulting non-Markovian master equation reads:

$$\frac{d}{dt}\rho_s(t) = -i[\Delta\sigma_{22} + \bar{\Omega}X_+, \rho_s(t)]$$
$$-\frac{\bar{\Omega}^2}{4}\sum_{i=+,-}\int_0^t d\tau\{G_i(\tau)[X_i, X_i(-\tau)\rho_s(t)] + \text{h.a.}\}, \tag{52}$$

with $X_+ = \sigma_{12} + \sigma_{21} = X_+^\dagger$ and $X_- = i(\sigma_{21}-\sigma_{12}) = X_-^\dagger$ to allow for a compact formulation of the master equation. The corresponding phonon Green's functions read $G_+(t) = \cosh[\phi(t)]-1$ and $G_-(t) = \sinh[\phi(t)]$. Interestingly, this trace-preserving master equation (after setting $\rho(t-\tau) = \rho(t)$) simulates the complex decoherence dynamics in more detail for time-independent system dynamics and poses a feasible alternative to time-convolutionless techniques [37, 140]. In the limit of a vanishing coupling element, one recovers the system dynamics without any contributions from the environment, as $G_\pm(t) \equiv 0$ and $\phi(t) = 0$, it follows $\Omega_R = \Omega$. The time dynamics of $X_i(\tau)$ is given via the electronic part of H_0. The general

solution for a detuned, driven two-level system reads with $\eta = \sqrt{4\Omega^2 + \Delta^2}$:

$$X_-(t) = \frac{2\Omega}{\eta}\sin(\eta t)X_z^0 + \cos(\eta t)X_-^0 - \frac{\Delta}{\eta}\sin(\eta t)X_+^0, \qquad (53)$$

$$X_+(t) = \frac{2\Omega\Delta}{\eta^2}[1 - \cos(\eta t)]X_z^0 + \frac{X_+^0}{\eta^2}[4\Omega^2 + \Delta^2\cos(\eta t)] + \frac{\Delta}{\eta}\sin(\eta t)X_-^0, \qquad (54)$$

$$X_z(t) = \left[\cos(\eta t) - \frac{\Delta^2}{\eta^2}[1 - \cos(\eta t)]\right]X_z^0 + \frac{2\Omega\Delta}{\eta^2}[1 - \cos(\eta t)]X_+^0 - \frac{2\Omega}{\eta}\sin(\eta t)X_-^0, \qquad (55)$$

where $X_i^0 = X_i(0)$ are the initial values and $X_z = \sigma_{22} - \sigma_{11}$ is given for completeness. Another interesting limiting case assumes $X_i(\tau) \approx X_i(0)$, that is, the system's dynamics is too slow and the environmental time correlation dominates the dissipative part of the master equation. As $X_+^2 = \mathbb{1} = X_i^2$ and $X_i(t) \approx X_i^0$, we can write

$$\sum_{i=+,-}\left\{G_i(\tau)[X_i, X_i(-\tau)\rho_s(t)] + \text{h.a.}\right\}$$

$$\approx 2\sum_{i=+,-}\text{Re}[G_i(\tau)][\rho_s(t) - X_i\rho_s(t)X_i]$$

$$= -\text{Re}[G_+(\tau) + G_-(\tau)][2\sigma_{12}\rho_s(t)\sigma_{21} + 2\sigma_{21}\rho_s(t)\sigma_{12} - 2\rho_s(t)]$$

$$-\text{Re}[G_-(\tau) - G_+(\tau)]\left[2\sigma_{12}\rho_s(t)\sigma_{12} + 2\sigma_{21}\rho_s(t)\sigma_{21}\right], \qquad (56)$$

which leads to the following master equation:

$$\frac{d}{dt}\rho_s(t) = -i[\Delta\sigma_{22} + \bar{\Omega}X_+, \rho_s(t)] + \Gamma_+(t)(\mathcal{D}[\sigma_{21}] + \mathcal{D}[\sigma_{12}])\rho_s(t) + \Gamma_-(t)(\sigma_{12}\rho_s(t)\sigma_{12} + \sigma_{21}\rho_s(t)\sigma_{21}) \qquad (57)$$

with the time-dependent damping and dephasing coefficients:

$$\Gamma_+(t) = \frac{\bar{\Omega}^2}{4}\text{Re}\left[\int_0^t d\tau(e^{\phi(\tau)} - 1)\right] \qquad (58)$$

$$\Gamma_-(t) = \frac{\bar{\Omega}^2}{4}\text{Re}\left[\int_0^t d\tau(e^{-\phi(\tau)} - 1)\right]. \qquad (59)$$

In Figure 7, we plot the solutions obtained from the polaron master equation in Eq. (57) in the weak driving limit $\Omega = 50\ \mu\text{eV}$ and the solution of the cluster expansion of second order from the set of equations in Eq. (31–36) for standard GaAs material parameter and $T = 77$ K. In the secular approximation $\Gamma_-(t) = 0$ and without the Rabi energy renormalization $\bar{\Omega} = \Omega$ in H_0 (left), the solutions agree well. Deviations with nonsecular terms and the renormalized Rabi energy become apparent even in the weak coupling, weak driving limit. However, the solution has been obtained in the very weak and resonant driving scenario. The advantage of the polaron master equation is the possibility to take into account dressed state dynamics in the case, when the time dependence of $X_i(\tau)$ becomes nonnegligible, however only up to driving strengths below the cut-off frequency as the polaron master equation does not allow to simulate dynamical decoupling scenarios.

An exemplary result is plotted in Figure 8. The experimental data points are obtained from self-assembled In(Ga,As)/GaAs QDs grown by metal–organic vapor-phase epitaxy. The corresponding sample includes a single layer of QDs centered in a 1-λ-thick planar GaAs cavity surrounded by alternating λ/4 periods of AlAs/GaAs as 4 top and 20 bottom distributed Bragg reflectors to enhance the photon extraction efficiency. A narrow band (500 kHz) tunable Ti:sapphire cw laser served as an excitation source, and the integrated intensity of an incoherently driven QD is compared with theory [50]. This detailed study of a
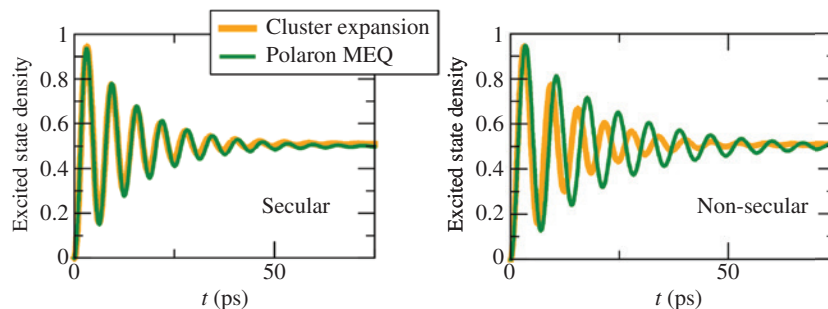

Figure 7: Comparison between the polaron master equation and cluster expansion solution in the second-order and weak driving limit ($\hbar\Omega = 50\ \mu\text{eV}$).
The solutions agree well without nonsecular terms and Rabi energy renormalization (left) for temperatures up to $T = 77$ K.
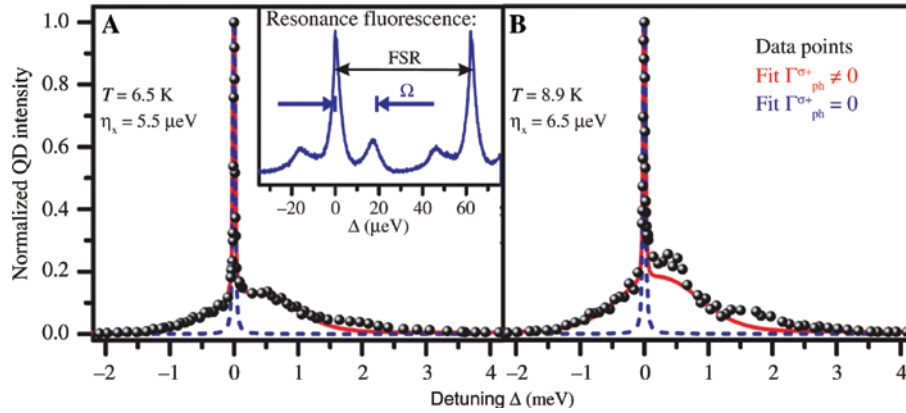
Figure 8: Integrated QD intensity derived from a frequency scan (black dots, experiment) and theory with (red) and without (blue) phonon-included processes on the basis of the polaron master equation for different temperatures (A) and (B).
Reprinted figure with permission from [50]. © 2012 by the American Physical Society.

phonon-assisted incoherent excitation mechanism of single QDs allows one to explore the underlying acoustic phonon bath dynamics and shows very good agreement with the polaron master equation theory. Please note that the experimental data points (black spheres) are only well produced, if the full phonon-induced quantum kinetics is taken into account such as in a polaron master equation model (red) with a constant external driving field and emerging additional incoherent excitation channels. Therefore, the QD coupling to the phonon reservoir does not only introduce pure dephasing and an enhancement of radiative decay processes, but also accounts for new and in Markovian models not included incoherent excitation/scattering channels if spectral detuning becomes important. The applied phonon-assisted incoherent excitation provides a unique excitation mechanism of a semiconductor QD and can be used as an effective new tool to map the characteristic features of the phonon bath present in such a solid-state quantum emitter system. Additional, it serves as an interesting quasiresonant excitation scheme for the triggered generation of single photons with high indistinguishability [26].

3.5 Phonon anticrossings in the Mollow regime (inductive equations of motion)

In addition to the perturbative models above, we address now numerically exact solutions. We start with the Heisenberg equation of motion approach, which can be used to calculate nonequilibrium phonon dynamics up to arbitrary order if an inductive equation of motion method is used. For example, for longitudinal optical (LO) phonons, the dispersion is constant in the Einstein approximation: $\omega(q) \equiv \omega_{LO}$ [24, 106, 141]. This allows for an

exact treatment of the electron–LO phonon interaction [28, 105, 106, 141]. Because of the constant dispersion, we may write the Hamiltonian in Eq. (7) in the interaction picture as $H_{e-p}^{lo}(t) = \sum_{q} f_{12}^{q}[b_{q}(t) + b_{q}^{\dagger}(t)] = B e^{-i\omega_{LO}t} + B^{\dagger} e^{i\omega_{LO}t}$. This leads to the commutation relation $[B(t), B^{\dagger}(t)] = |f|^{2}$ with $|f|^{2} = \sum_{q} |f_{12}^{q}|^{2}$, which corresponds to the renormalized harmonic oscillator picture. This collective operator leads to a numerically exact solvable set of equations. Using the Heisenberg equation of motion for a nonexplicit time-dependent operator: $-i\hbar \frac{d}{dt} A = [H_{e-l}^{sc} + H_{e-p}^{lo}, A]$ from Eqs. (2) and (7), a set of differential equations, defining $\langle A^{n,m} \rangle = \langle A B^{\dagger n} B^{m} \rangle$, can be derived. As an example, we give the full set of equations of motion for a driven QD with LO phonon interaction:

$$\frac{d}{dt}\langle \sigma_{12}^{n,m} \rangle = -i(\omega_{21} - (n-m)\omega_{LO} - i\Gamma/2)\langle \sigma_{12}^{n,m} \rangle$$
$$- i\Omega(t)(2\langle \sigma_{22}^{n,m} \rangle - \langle \mathbb{1}^{n,m} \rangle) - i\sum_{q} f_{12}^{q}(\langle \sigma_{12}^{n+1,m} \rangle + \langle \sigma_{12}^{n,m+1} \rangle)$$
$$- i(1 - \delta_{n,0})n|f|^{2} \sum_{q} f_{12}^{q}\langle \sigma_{12}^{n-1,m} \rangle, \tag{60}$$

$$\frac{d}{dt}\langle \sigma_{22}^{n,m} \rangle = -(\Gamma - i(n-m)\omega_{LO})\langle \sigma_{22}^{n,m} \rangle$$
$$+ 2\mathrm{Im}[\Omega(t)\langle \sigma_{12}^{n,m} \rangle] - i\sum_{q} f_{12}^{q}(\langle \sigma_{22}^{n+1,m} \rangle + \langle \sigma_{22}^{n,m+1} \rangle)$$
$$+ i(1 - \delta_{n,0})n|f|^{2} \sum_{q} g_{12}^{q}\langle \sigma_{22}^{n-1,m} \rangle$$
$$- i(1 - \delta_{m,0})m|f|^{2} \sum_{q} f_{12}^{q}\langle \sigma_{22}^{n,m-1} \rangle, \tag{61}$$

$$\frac{d}{dt}\langle \mathbb{1}^{n,m} \rangle = i(n-m)\omega_{LO}\langle \mathbb{1}^{n,m} \rangle + i(1 - \delta_{n,0})n|f|^{2} \sum_{q} f_{12}^{q}\langle \sigma_{12}^{n-1,m} \rangle$$
$$- i(1 - \delta_{m,0})m|f|^{2} \sum_{q} g_{12}^{q}\langle \sigma_{12}^{n,m-1} \rangle. \tag{62}$$

This set of equation is complete and allows one to solve the dynamics of the coupled phonon-emitter system and calculate the associated emission spectra, cf. Figure 9. Note that with given initial conditions and for a fixed time interval, hierarchies only up to a certain N in the phonon interaction contribute. This maximum N is tested until convergence is reached, depending on the time interval and coupling strength of the system. This inductive equation of motion method has been applied, for example, to calculate the luminescence spectrum of a strongly driven QD with LO phonon satellite peaks [107]. Because of the present electron–LO phonon interaction, the typical Mollow triplet is changed and additional side peaks appear at the frequency of the LO phonon satellite peaks 36 meV. In Figure 9, an emission scheme is depicted showing that besides the strong drive-induced Mollow sideband, also LO phonon emission and absorption occurs and introduces Raman-like features into the spectrum under coherent excitation. Another important aspect is the fact that the phonon emission and absorption is strongly temperature-dependent. Here, the temperature is included in the initial conditions for the expectation values: $\langle B^{\dagger n}(0)B^m(0)\rangle = \delta_{nm} n![\exp(\beta\hbar\omega_{LO})-1]^{-1}$ and $1/\beta = k_B T$. For low temperatures, because of the LO phonon frequency in the range of for example, $\hbar\omega_{LO} = 36$ meV, spontaneous emission dominates, leading to strong Stokes contributions. Given the set of equations of motions, the dynamics of the coupled laser-QD system can be calculated and because of the included Markovian radiative decay constant Γ, a steady state is inevitably reached. Via a two-time correlation function, using the quantum regression theorem [35, 36, 38], the power spectrum $S(\omega)$ is obtained. In Figure 9, the power spectrum of a QD under cw excitation $\Omega(t) = \text{const}$ is

plotted for different Rabi energies Ω. Clearly, for low-excitation amplitudes, the Mollow triplet can be identified and an additional LO phonon satellite peak triplet becomes visible, where both scale linearly with the Rabi energy. Interestingly, if the excitation strength becomes comparable with the LO phonon energy, anticrossings occur and both, the electronic and phononic triplet interfere, forming a new Eigenstate [107]. This has the interesting practical consequence that the splitting allows one to obtain independently and spectrally resolved the electron–phonon interaction strength without relying on the delicate measurement of the relative peak heights [43, 142, 143] to estimate the Huang–Rhys factor $F_{HR} = \sum_{\mathbf{q}} |f_{12}^{\mathbf{q}}|^2 / \omega_{LO}^2$.

3.6 Phonon-assisted population inversion (real-time path integral)

Because of the intrinsic non-Markovian nature of the electron–phonon dynamics, perturbation approaches such as reviewed above break down either in the high temperature or strong coupling limit. With exception of phonon modes with constant dispersion, in which the Heisenberg inductive equations of motion are numerically exact, only the real-time path integral method is capable to treat the coupling of QDs to a continuum of acoustic phonons exactly for time-dependent excitation scenarios. This method relies on slicing the time evolution into discrete steps and is similar to recently widely used time-evolving block decimation or matrix-product state methods [111, 112, 114, 115, 144]. These models take into account not only the non-Markovian features of the system dynamics but also the growing degree of entanglement between system
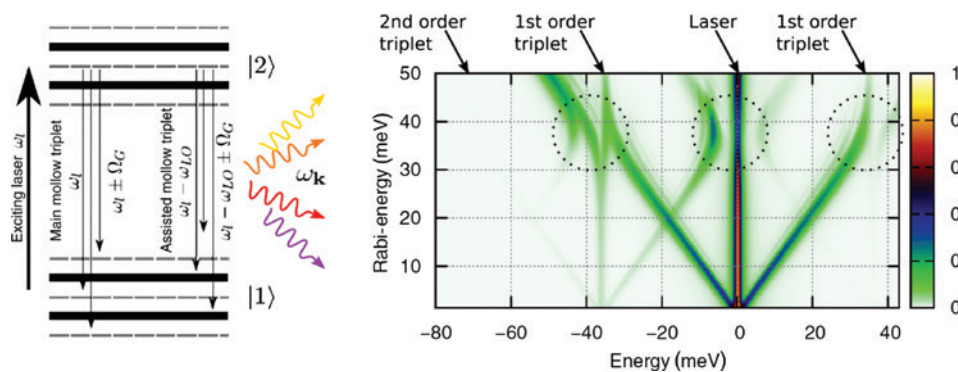

Figure 9: Scheme and power spectrum of a two-level system (e.g. QD) interacting coherently with strong external laser field. The emission consists of triplets centered at the driving laser frequency (Mollow triplet) and at the Raman frequencies (only Stokes contribution shown). For driving strength of the order of the LO phonon energy, additional anticrossings occur. © 2011 American Physical Society, reprinted from [107].

and reservoir states because of excitation exchange and information backflow.

The real-time path integral method is derived from the Caldeira–Leggett model [110] and has been reviewed widely within the well-known spin-boson problem [33, 115, 145]. The application to the QD–phonon kinetics has been successfully applied to exciton [33] and biexciton systems [47]. Interestingly, the real-time path integral method has also successfully used to describe phonon-induced dephasing in a coherently coupled QD microcavity systems in the regime of cavity quantum electrodynamics (cQED) with efficient numerical protocols [116, 117].

Starting point is the general solution of the Liouville–von Neumann equation:

$$\rho(t) = T\left\{\exp[-i\int_0^t H(t')dt']\right\}\rho(0)\left[T\left\{\exp[i\int_0^t H(t')dt']\right\}\right]^\dagger, \quad (63)$$

In contrast to Section 3.1, we take light–matter interaction into account: $H(t) = H_{e-l}^{sc}(t) + H_{e-p}^{LA}$. Choosing a final QD state, we are interested in $|i_N\rangle\langle i_N'|$ at time $t = N\Delta t$, and summing overall possible initial system and phonon and final phonon states in the coherent state representation, we yield:

$$\langle i_N | \rho^s(t) | i_N'\rangle = \iiint \frac{d^2 z_N}{\pi}\frac{d^2 z_0}{\pi}\frac{d^2 z_0'}{\pi}\langle z_N, i_N | U(t, 0) | z_0, i_0\rangle \quad (64)$$

$$\langle z_0, i_0 | \rho(0) | z_0', i_0'\rangle\langle z_0', i_0' | U^\dagger(t, 0) | z_N, i_N'\rangle \quad (65)$$

We proceed as before when we derived the independent boson model in Eq. (25) and trace out the system degrees of freedom first. We use a stroboscopic evolution in time slices Δt, applying the Suzuki–Trotter decomposition and trivially fulfilling the time-order in doing so. Then, we insert between the time slices (N-1)-times the system identity $\mathbb{1} = \sum_{i_n=1,2}|i_n\rangle\langle i_n|$ and yield following matrix elements:

$$\langle i_n | \exp[-iH(n)] | i_{n-1}\rangle = \langle i_n | \exp[-iH_{e-l}^{sc}(n)] | i_{n-1}\rangle$$
$$\exp[-iH_{e-p}^{LA}(n, i_{n-1})], \quad (66)$$

where we assumed Δt to be small that the electron–phonon and light–matter Hamiltonian commute to first order, and we exploit the fact that electron–phonon interaction is diagonal in the system states. The light–matter interaction reads explicitly (for resonant excitation):

$$\langle i_n | \exp[-iH_{e-l}^{sc}(n)] | i_{n-1}\rangle = M_{i_{n-1}}^{i_n}$$
$$= \langle i_n | \begin{bmatrix} \cos[f_n] & -i\sin[f_n] \\ -i\sin[f_n] & \cos[f_n] \end{bmatrix} | i_{n-1}\rangle, \quad (67)$$

reducing the system dynamics to c-values per time slice and $f_n = \int_{(n-1)\Delta t}^{n\Delta t}\Omega(t)dt$. Now, the electron–phonon interaction is reduced to a Gaussian problem and the Feynman–Vernon influence functional can be derived. It is convenient to use the coherent state representation, inserting (N-1)-times the phonon subspace identity, the evolution reads:

$$\langle z_N, i_N | U(t, 0) | z_0, i_0\rangle = \prod_{n=1}^N M_{i_{n-1}}^{i_n}\int \mathcal{D}Z T[e^s] \quad (68)$$

with S as the phonon action and formally as a path integral with corresponding trajectories for Gaussian degrees of freedom. Taking the extremum, solving for the classical equation of motion for the phonon degrees of freedom, and tracing out the phonon reservoir, one yields the reduced density matrix evolution:

$$\langle i_N | \rho^s(t) | i_N'\rangle = \prod_{n=1}^N M_{i_{n-1}}^{i_n}\left(M_{i_{n-1}'}^{i_n'}\right)^*\prod_{m=1}^n e^{-S_{nm}}\langle i_0 | \rho^s(0) | i_0'\rangle \quad (69)$$

where the impact of the phonon reservoir is included via:

$$S_{nm} = \int_{n-1\Delta t}^{n\Delta t}dt_1\int_{m-1\Delta t}^{m\Delta t}dt_2(i_n - i_n')[\phi(t_1 - t_2)i_m - \phi^*(t_1 - t_2)i_m'] \quad (70)$$

for $k \neq m$ as an example with the phonon correlation $\phi(t)$ given in Eq. (50). Note, the solution assumes a real phonon coupling element and a two-level system in which the phonons couple to the excited state only. We recover the solution of the independent boson model when $\Omega(t) \equiv 0$ and $i_0 \neq i_0'$,

$$\langle 2 | \rho_{IBM}^s(N\Delta t) | 1\rangle = \prod_{n=1}^N\prod_{m=1}^n e^{-S_{nm}}\langle 2 | \rho^s(0) | 1\rangle \quad (71)$$

leading numerically to solution given in Section 3.1 in Eq. (25).

In principle, the problem is solved with Eq. (69). However, the evaluation is numerically still expensive and can be reduced strongly by taking into account an "on fly" screening [33, 146, 147] because of the fact that for longitudinal acoustic phonon coupling (or other superohmic environments), the memory falls off rapidly. Furthermore, boundary conditions need to be imposed to recover known exact solutions [33, 146, 147]. This exact method can also be used to benchmark perturbative approaches. In Figure 10 and in Ref. [108], the cluster expansion solution of the second-order (orange line) is compared with the numerically exact solution from the real-time path integral method (green line). As a figure of merit, the real part of the microscopic coherence is calculated for a QD
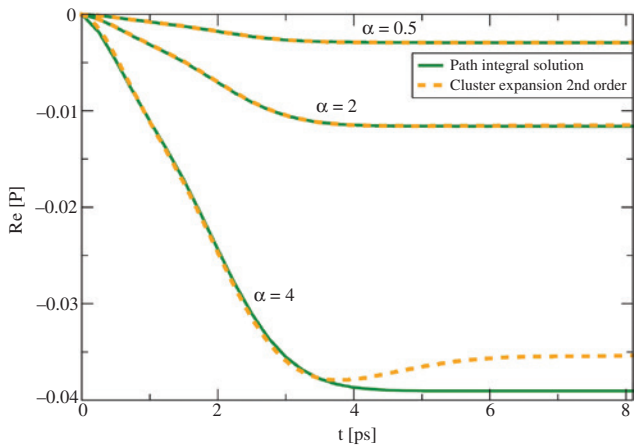
Figure 10: Comparison of the real time path-integral solution with the cluster expansion time-trace for cw excitation.
Clearly, for weak coupling ($\alpha < 2$), the cluster expansion solution of second-order (orange) captures the correct steady-state of the real part of the microscopic coherence $P < \sigma_{12}$. However, for stronger coupling and elevated temperatures deviations arise, and only the path-integral solution (green) predicts the correct experimental values.

exposed to a weak cw driving. Due to the electron-phonon interaction, the Eigenstate of the system change and a real part of the coherence emerges in dependence on the driving and the electron-phonon coupling strength. This real part saturates fast and captures intrinsical phonon-induced effects.

Clearly, for weak coupling (g_{12}^q), that is, the standard semiconductor GaAs parameters, i.e. $\alpha < 2$, the path integral solution, and the cluster expansion are in agreement for low temperatures, e.g. $T = 4$ K. For a stronger coupling, e.g. $\alpha \geq 4$, the deviation is visible and a clear breakdown of

the cluster expansion solution is recognizable, and unrealistical oscillations may occur (not shown).

Full demonstration of the reliability of the path integral method has been achieved in population inversion protocols where the laser pulses are tuned within the neutral exciton phonon sideband [25]. This unconventional method achieves the inversion by rapid thermalization of the optically dressed states for which incoherent phonon-assisted relaxation processes are necessary. In Figure 11, the exciton population $\text{Tr}_B[\langle 2 | \rho(t) | 2 \rangle]$ is plotted (experiment b; theory c). The experimental data have been obtained from a layer of InGaAs/GaAs QDs embedded in the intrinsic region of an n-i-Schottky diode structure at 42 K, where the measured photocurrent is the quantity of interest to measure the final occupation of the exciton state. We observe a very good overall agreement between experiment and theory, and all qualitative features are reproduced and confirmed by microscopic input parameters. The population inversion arises due to the incoherent phonon-induced relaxation between optically dressed states, and the occurring phonon scattering becomes an enabling factor in the high driving limit.

4 Nonequilibrium phonon dynamics in quantized light–matter interaction

Quantum optical experiments based on solid-state quantum emitter platforms have made significant advances over the past decade. Manifestly atomlike
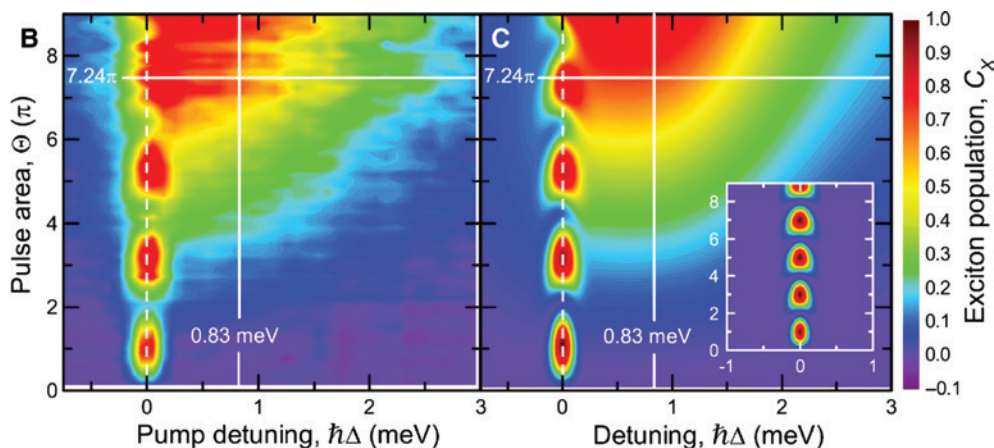

Figure 11: Experimentally obtained (left, B) exciton population versus the pulse area and laser detuning. The path integral solution is given in (C, right) and in very good agreement with the measured signal. The inset (C) shows the calculated values without electron–phonon interaction. Reprinted figure with permission from [25]. © 2015 by the American Physical Society.

properties have been demonstrated for semiconductor QDs, and further progress is expected from coupling those semiconductor nanostructures to microcavities as development of in situ lithography techniques advances rapidly [148, 149]. Related progress in the fabrication of QD microcavities paves the way to use the Purcell effect in the optical regime to build efficient and deterministic sources of single photons with tunable photon statistics [150, 151]. Exploiting such phenomena, QDs coupled to a cavity mode become even more atomlike [6, 100, 152–155]. Many well-known features of AOM physics have already been demonstrated on solid state–based platform such as Rabi splitting [6] or spectral Jaynes–Cummings ladder signatures [153, 156, 157]. In contrast to atoms, solid-state environments are also tailorable and provide the possibility to position nanostructures on demand such as QDs permanently in a high-Q microcavity [20], cf. Figure 12. Independent on natural given atomic features, the size and geometry of the QD are controlled properties, for example, the coupling strength and the confinement energies [58]. Those systems are scalable and perform as material platforms for future technological applications, including single-photon emitters [1, 158–160]. However, compared with atomic systems, quantum emission features in semiconductor nanostructures are ultimately accompanied with decoherence and scattering in the

Figure 12: Scanning electron micrograph of a pillar with a diameter of about 0.8 mm.
A combination of electron beam lithography and reactive dry etching allows one to obtain micropillars with close to vertical and defect-free sidewalls. Figure reprinted from [6].

semiconductor environment [161, 162], as also we have reviewed in Section 3(A–F).

In this section, we selectively review phonon-induced phenomena in cQED based on QDs as active medium and where the quantized nature of the light field enters in the description of the dynamics. The following examples are ordered from the single- via the two- to the many-photon regime. First (Section 4.1), we extend the theoretical toolbox by introducing the time-convolutionless method to model the Jaynes–Cummings physics in the single-excitation limit via H_{e-l}^{cav} in Eq. (3) and show that acoustic phonons introduce dephasing but also a Rabi frequency renormalization via H_{e-p}^{LA} [117, 163]. In this single-photon regime, two aspects of the semiconductor environment in QD-based cQED are given, for example, disadvantageous impact of phonons on the goal to reach the strong coupling regime [163]. Furthermore, and also in the single-photon limit, phonon-mediated cavity feeding is discussed, an interesting effect that strongly deviates from the idealized "artificial atom" model typically applied [80, 164–166].

In the two-photon limit (Section 4.2), we discuss the emission of photon pairs into free space, based on H_{e-l}^{con}. In this quantum optically nonlinear regime, we discuss the effect of colored noise in H_{e-p}^{st} on the visibility of subsequently emitted photons in a Hong-Ou-Mandel setup. This colored noise can be interpreted as semiclassically treated phonon influence as in Section 3.1 when the susceptibility has been derived. We demonstrated that changing the pulse separation in a two-pulse sequence allows one to monitor environmental correlations and unravels the intrinsic memory kernel [167]. Overall, the semiconductor environment is inevitably involved in excitation processes and renders coherent excitation processes partially incoherent, which are nevertheless crucial for a quantitative understanding of experimental results. However, as mentioned already above, the same environment, which has detrimental effects on the coherence, may also in certain scenarios become advantageous and supports quantum optical properties.

As an example of phonon-assisted coherence increase, we discuss in Section 4.3 the collapse and revival phenomenon known from AMO physics based on the Jaynes–Cummings model Hamiltonian H_{e-l}^{cav}. Here, we use the inductive equations of motion approach from Section 3.5 to model a QD strongly coupled to microcavity mode, which is initialized in a coherent state. This coherent state leads to the collapse and revival phenomenon [36, 168, 169]. Typically, for low photon numbers, the collapse and revival patterns vanish fast into an irregular oscillatory behavior, but a QD coupled to an acoustic
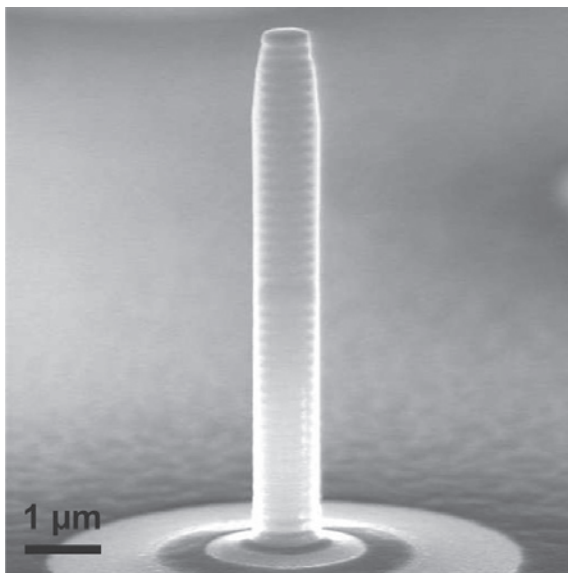
phonon reservoir exhibits a stabilization via H_{e-p}^{LA} and the collapse and revival phenomenon survives much longer in the presence of phonon-mediated coherence support [29]. Therefore, we show before concluding this review that phonon nonequilibrium dynamics may even be supported and enhanced quantum coherences.

4.1 Phonon-induced decoherence in QD-cQED

There is a wide range of examples how scattering processes limit the performance of semiconductor nanostructures [7, 11, 12, 154]. To take into account the underlying non-Markovian physics of the phonon environment, simulations must rely either on higher-order perturbative Markovian approaches, time-convolutionless techniques, highly numerically expensive nonequilibrium Green's function models, or exact diagonalization. Here, the influence of the non-Markovian is calculated using a time-convolutionless approach [37, 140]. Given the dynamics of the reduced density matrix in second order of the electron–phonon interaction Eq. (39), the system density matrix is approximated in a timelocal form by setting $\rho(t-\tau) \approx p(t)$. Using the full Hamiltonian H including the cavity–QD interaction H_{e-l}^{cav}, the dynamics in the single excitation limit yield the following set of equations of motion, if the photon-assisted ground state is abbreviated with $c^\dagger \sigma_{11}^{QD} c =: \sigma_{11}$:

$$\frac{d}{dt}\langle\sigma_{22}\rangle = -\Gamma\langle\sigma_{22}\rangle + 2\text{Im}[g\langle\sigma_{12}\rangle], \tag{72}$$

$$\frac{d}{dt}\langle\sigma_{12}\rangle = -[\Gamma/2 + \kappa/2 + i\Delta - A(t)]\langle\sigma_{12}\rangle \\ -[B(t)+ig]\langle\sigma_{11}\rangle + [C(t)+ig]\langle\sigma_{22}\rangle, \tag{73}$$

$$\frac{d}{dt}\langle\sigma_{11}\rangle = -\kappa\langle\sigma_{11}\rangle - 2\text{Im}[g\langle\sigma_{12}\rangle] \tag{74}$$

where a Markovian radiative decay and a cavity loss is assumed $\kappa\mathcal{D}[c]\rho$ and a detuning between cavity mode and the QD is assumed with $\Delta = \omega_{21} - \omega_c$. The influence of the acoustic phonons is included in the time-dependent coefficients A, B, C, obtained after inserting a unity in the time-local master equation:

$$A(t) = \int_0^t d\tau[\phi_I(\tau)\langle 1|\sigma_{22}(-\tau)|1\rangle - \phi_I^*(\tau)\langle 2|\sigma_{22}(-\tau)|2\rangle], \tag{75}$$

$$B(t) = \int_0^t d\tau \phi_I^*(\tau)\langle 1|\sigma_{22}(-\tau)|2\rangle, \tag{76}$$

$$C(t) = \int_0^t d\tau \phi_I(\tau)\langle 1|\sigma_{22}(-\tau)|2\rangle, \tag{77}$$

with $\langle i|\sigma_{22}(-\tau)|j\rangle = \langle i|U(\tau, 0)|2\rangle\langle 2|U(-\tau, 0)|j\rangle$ the time-evolution matrix element of the unperturbed system with time evolution operator: $U(t, 0) = \exp[-igt(\sigma_{12}+\sigma_{21})-i\Delta t]$, and $\phi_I(t)$ is given in Eq. (26). $A(t)$ includes the polaron shift and the dephasing dynamics via the imaginary and the real part, respectively. $B(t)$ and $C(t)$ renormalize the interaction strength between the cavity mode and the QD via the independent boson phonon correlation function. This is an important feature of non-Markovian open quantum system dynamics, as a system–reservoir coupling introduces an increase of entanglement and thermalization at the same time, leading to a loss of information and basically new "dressed" system states. In the Markovian limit $\phi(t) \to \gamma_p\delta(t)$, we recover a Lindblad type of interaction, in which $B(t)$ and $C(t)$ are vanishing because of $\langle i|j\rangle = \delta_{ij}$ and $A(t)$ reduces to $-\gamma_M$ in which all phonon characteristics are gone and a phenomenological pure dephasing constant remains.

The formulation with finite time kernel, however, allows one to investigate the phonon impact on the strong coupling regime of the QD-cQED without overestimating the dephasing rate, which is the case for a Markovian decay. A figure of merit for the strong coupling regime is a nonmonotonic decrease of the initial QD occupation $\langle\sigma_{22}(0)\rangle = 1$ with $\langle\sigma_{22}(t_1)\rangle \geq \langle\sigma_{22}(t_2)\rangle$ for $t_2 > t_1$. Figure 13 shows the parameter space where strong coupling and weak coupling resides depending on the bare coupling constant g and the temperature. The temperature enters in the phonon correlation function via $\phi(t) \equiv \phi(t, T)$. From evaluating the dynamics in the single-excitation regime, it becomes apparent that the higher the temperature, the stronger must be the cavity–QD coupling to yield nonmonotonous decay dynamics of the QD excitation [34]. Remarkably, the coupling–renormalization has a strong effect (without renormalization dashed lines, with renormalization solid
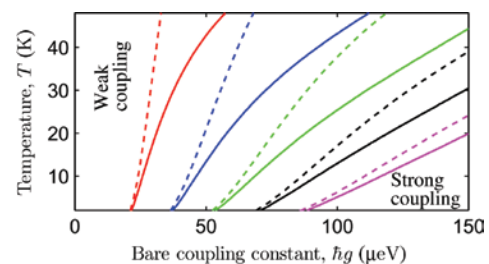

Figure 13: Parameter space where strong coupling and weak coupling resides for QD-based cQED depending on the bare coupling constant and the temperature.
Non-Markovian phonon interaction leads to a renormalization and affects strongly the transition from weak to strong coupling (solid lines with renormalization, dashed lines without). Reprinted figure with permission from [163]. © 2010 by the American Physical Society.

lines). This energy renormalization is also important in explaining asymmetries in life times with respect to the QD–cavity detuning in cavity feeding scenarios.

A pronounced increase in a nonresonant QD–cavity coupling toward elevated temperatures is a strong indication of phonon-mediated relaxation processes [51, 54, 164]. The spectral mismatch between the cavity mode and the emitter is then bridged by either phonon emission if the emitter is blue detuned from the cavity mode, or phonon absorption if the emitter field is red detuned. This asymmetry is included in the phonon correlation function $\phi(t)$ and not included in the Markovian limit, where $\phi(t) \to \gamma_M \delta(t)$. As for low temperatures, $n_q \to 0$ processes accompanied by phonon emission ($n_q + 1$) are favored over those obtained by phonon absorption (n_q), and spectral asymmetries become visible and pronounce in this temperature regime. In Figure 14, the non-Markovian relaxation dynamics of a detuned QD–cavity QED platform is investigated [80] and given in the single excitation as:

$$\frac{d}{dt}\langle \sigma_{11} \rangle \approx 2g^2 \text{Re}\left[\int_0^\infty d\tau e^{i\Delta\tau - \phi(\tau)}\right]\langle \sigma_{22} \rangle, \qquad (78)$$
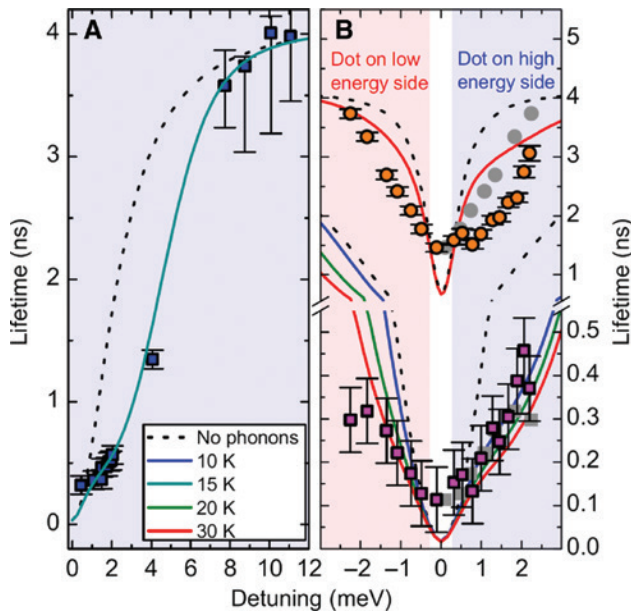

Figure 14: Extracted decay times of a QD–cavity system as a function of detuning.
Experimental data (dots) are in good agreement with non-Markovian phonon theory (solid line) in comparison without phonons (dashed lines). Figure (A) shows that neglecting the phonon contributions leads only in the small and large detuning limit the experimentally correct excitonic lifetimes, whereas including phonons allows to correctly mediate between these limits. In (B), there are two sets of data. Squares refer to the fast and circles to the slow components of the luminescence decay. Reprinted figure with permission from [80]. © 2009 by the American Physical Society.

if instead of the phonon interaction, the cavity–QD interaction is taken as a perturbation up to second order in the reduced but timelocal density matrix, cf. Eq. (39). This transition strength from excited to ground state can be understood as a generalization of Fermi's golden rule [37, 51]. A model without phonons (dashed line) cannot reproduce the effective lifetimes of the coupled QD–cavity system as a function of the detuning Δ (experimental data, dots). The non-Markovian simulations (solid) were computed with a measured quality factor $Q = 2900$ and a cavity–QD coupling strength $\hbar g = 45$ µeV. Also, the asymmetric dip of the lifetime with respect to the detuning is not reproduced without phonon dynamics, showing that phonon-mediated feeding cannot be captured with a broadened zero-phonon linewidth. For higher excitation manifolds, it can furthermore be shown that the cavity feeding effect depends nontrivially on the detunings, for example, maximal efficiency is obtained for detunings corresponding to transition energies between cavity-dressed states with excitation numbers larger than one [116]. Quantum correlations, such as entanglement and indistinguishability, however, still decohere because of phonon-induced noise, as will be discussed next.

4.2 Hong-Ou-Mandel effect: photon indistinguishability

A good figure of merit to characterize the noise robustness of a quantum emitter is the two-photon coherence such as in Hong-Ou-Mandel (HOM) type of experiments [170]. If the photon–photon correlation function of two photons subsequently emitted from a single emitter [5] is strongly antibunched after interfering in a Hanbury Brown and Twiss setup, the quantum emitter is time-translational robust and shows therefore no noise. Such quantum optical experiments probe therefore the indistinguishability of emitted photons and are the basis for entanglement distribution via Bell-state measurements in long-distance quantum communication networks [81, 82]. Because the visibility on HOM interference experiments is influenced by the dephasing of the quantum emitters, they are well suited to explore decoherence on the nanoseconds timescale under variation of, for instance, the temperature with high sensitivity. In the theoretical description of HOM experiments, we extend the single-mode cavity Hamiltonian in Eq. (3) to a multimode description H_{e-l}^{con} in Eq. (4). Furthermore, we model the phonon contribution with a stochastic force $F(t)$ via H_{e-p}^{st} in Eq. (5) to solve the problem analytically. To probe decoherence on a nanoseconds timescale, the QD is excited with a two-pulse sequence with variable pulse separation

δt. The first pulse creates an excitation via resonant p-shell excitation, which radiatively decays under emission of a photon from the s-shell of the QD. After a time delay δt in which the QD may experience a reconfigured charge environment slightly shifting its energy levels, a second pulse creates another excited state within the QD and another photon is subsequently emitted. The corresponding two-photon wave function reads:

$$|\Psi\rangle = E_L^{(-)}(\infty, 0)E_S^{(-)}(\infty, \delta t)|\text{vac}\rangle$$
$$E_n^{(-)}(t, \tau) = -ig\int_0^\infty d\omega_n \int_\tau^t dt' e^{i(\omega_n - \omega_{21})t' - i\Phi_\tau(t') - \Gamma t'} c_{\omega_n}^\dagger. \quad (79)$$

We distinguish channels with the labels: ω_L for long ω_S for short, that is, the photons are distinguishable via their spatial traveling mode in the detection path until they superpose at the HOM beam splitter. Note the difference in the lower limit of the integrals (0, δt) and in the integrated noise signals $\Phi_\tau(t) = \int_\tau^t dt' F(t')$, and the radiative decay constant is given with $\Gamma = g^2\pi$. If the first photon now takes a longer way to the 50:50 HOM beam splitter with single-photon detectors A and B at its two output ports and the second photon travels the shorter route, both photons can interfere

$$\sqrt{2}E_A^{(\pm)} := E_S^{(\pm)} + E_L^{(\pm)},$$
$$\sqrt{2}E_B^{(\pm)} := E_L^{(\pm)} - E_S^{(\pm)}. \quad (80)$$

In this case, the detected photon–photon correlation gives a direct measure for the degree of indistinguishability in terms of the HOM visibility as discussed in the following.

The unnormalized HOM two-photon correlation function reads:

$$G^{(2)}(t_D, t_D + \tau) = \langle\langle|E_B^{(+)}(t_D + \tau)E_A^{(+)}(t_D)|\Psi(t)\rangle|^2\rangle\rangle$$
$$= \frac{2\Gamma^2}{(2/\pi)^2} e^{-\Gamma(2t_D+\tau)} \langle\langle 1 - \text{Re}[e^{-i\xi(t_D, \tau, \delta t)}]\rangle\rangle, \quad (81)$$

with the noise contribution $\xi(t_D, \tau, \delta t) = \Phi_0(t_D + \tau) + \Phi_{\delta t}(t_D) - \Phi_{\delta t}(t_D + \tau) - \Phi_0(t_D)$. The two-photon correlation function vanishes in case of indistinguishable photon emission events, that is, for vanishing noise $\xi \equiv 0$ or infinite correlated noise: $\Phi_{\delta t}(t) = \Phi_0(t)$. This is the expected result, which implies that if the emitter is not subjected to a varying environment or negligible environment influence at all, the emitted photons are indistinguishable as the emission event is time-translational invariant. However, in the typical experimental setting with finite noise contribution, for example, because of charge noise by access electron and holes under nonresonant excitation,

fluctuating surface charges, and/or electron–phonon scattering, decoherence occurs and reduces the HOM visibility. The figure of merit and experimentally accessible quantity is again the HOM visibility:

$$V(\delta t) = 1 - \int_0^\infty \int_0^\infty d\tau dt \frac{G^{(2)}(t, \tau)}{(\pi/2)^2}. \quad (82)$$

Note, the pulse delay and noise contribution are still present in the two-photon correlation. If a delta-correlated white noise is assumed, that is, in the situation when the noise correlation of different emission events vanishes identically, we obtain:

$$V(\delta t, \tau_c)|_{\text{Markovian}} = 1 - \frac{\gamma}{\Gamma + \gamma} = \frac{\Gamma}{\gamma + \Gamma}. \quad (83)$$

This is an interesting result that deserves further explanation. Firstly we note that here the photon indistinguishability is independent from the radiative decay constant (as a Markovian radiative decay process has been assumed) but depends strongly on the pure dephasing processes within the emission processes. However, for a Markovian decoherence process, the reduced visibility does not depend on the delay between the two pulses in a two-pulse sequence. Thus, a non-Markovian treatment needs to established to fully capture the complexity of the two-pulse experiment and its underlying physics. To illustrate and substantiate this statement, we consider experimental results on the HOM visibility of a semiconductor QD presented in Figure 15A and B, where the QD is excited in a two-photon sequence with different pulse delays δt. The HOM visibility clearly decreases with increasing pulse
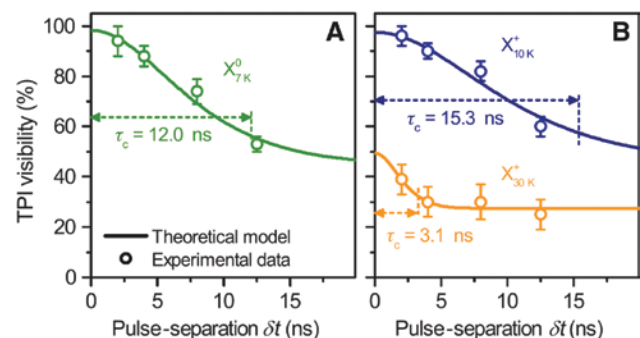

Figure 15: Two-photon interference visibilities of consecutively emitted single photons in dependence on the pulse separation δt. Experimental data for (A) the neutral exciton state and (B) the charged exciton state are quantitatively described by a theoretical model assuming a non-Markovian noise correlation, leading to spectral diffusion on a nanosecond timescale. Reprinted figure with permission from [167]. © 2016 by the American Physical Society.

separation, and a Markovian model cannot be applied to model this result. In contrast, a colored noise model with a phenomenologically assumed correlation length of the emission events allows us to characterize the emitter for given visibility data. For this purpose, we include this dependence as a finite memory effect with specific correlation time of τ_c:

$$\langle\langle\Phi_{t_1}(t_2)\Phi_{t_3}(t_4)\rangle\rangle = \Gamma' e^{-\frac{(t_1-t_3)^2}{\tau_c^2}} (\min[t_2, t_4] - \max[t_1, t_3]). \quad (84)$$

This kind of noise correlation stems from a non-Markovian low-frequency noise [171–173] and shows plateau-like behavior for temporal pulse distances sufficiently short in comparison with the experimentally extracted memory depth. With the correlation length parameter, we derive for the visibility:

$$V(\delta t, \tau_c) = \frac{\Gamma}{\gamma(1 - \exp[-(\delta t/\tau_c)^2]) + \Gamma}. \quad (85)$$

Therefore, for vanishing pure dephasing the visibility is 1, that is, consecutively emitted photons are Fourier transform limited and coalesce at the beamsplitter into a perfect coherent two-photon state. Further dephasing could also be suppressed by strict resonant excitation [159], electrical charge control [22], or suitable surface passivation [174]. A detailed understanding of effects limiting the HOM visibility in two-pulse experiments is of vital interest for the further development of state-of-the-art QD-based quantum light sources toward the implementation of quantum circuits, for example, boson sampling and advanced quantum communication protocols such as measurement device independent quantum key distribution and the quantum repeater. This challenging goal can only be achieved by engineering and operating the sources to effectively suppress phonon-induced dephasing and spectral diffusion at timescales well beyond the nanosecond range in the future.

4.3 Phonon-enhanced coherence

Lattice vibrations in semiconductor QDs give rise to new effects not known in atomic quantum optics such as phonon-mediated off-resonant cavity feeding (Section 4.1), formation of phonon-assisted Mollow triplets [107] and temperature-dependent vacuum Rabi splittings in cavity emission spectra [117]. Expanding on these developments, another example is phonon-induced quantum optical coherence [29, 49]. Here, the memory

effects of the phonon bath are investigated with respect to its impact on quantum optical pattern formations in the coherent collapse and revival phenomenon. This expands the non-Markovian investigation beyond the single excitation limit, as higher-order photon manifolds are involved.

The basis of the investigation is the inductive Heisenberg equation of motion approach [28, 105], presented in Section 3.5. The cavity–QD dynamics (H_{e-l}^{cav}) is calculated within a numerically exact approach, while the coupling to the longitudinal acoustic phonon reservoir (H_{e-p}^{LA}) is treated for every photon manifold at second-order Born level. The corresponding equations of motion read for resonant interaction between QD and cavity photons $\Delta = -\Delta_p$ to compensate for the polaron shift:

$$\frac{\mathrm{d}}{\mathrm{d}t}\langle c^{\dagger m}c^m\rangle = -2m\kappa\langle c^{\dagger m}c^m\rangle - 2m\,\mathrm{Im}[g\langle\sigma_{12}c^{\dagger m}c^{m-1}\rangle] \quad (86)$$

$$\frac{\mathrm{d}}{\mathrm{d}t}\langle\sigma_{22}c^{\dagger m}c^m\rangle = -2m\kappa\langle\sigma_{22}c^{\dagger m}c^m\rangle + 2m\,\mathrm{Im}[g\langle\sigma_{12}c^{\dagger m+1}c^m\rangle] \quad (87)$$

$$\frac{\mathrm{d}}{\mathrm{d}t}\langle\sigma_{12}c^{\dagger m+1}c^m\rangle = -[(2m+1)\kappa - i\Delta]\langle\sigma_{12}c^{\dagger m+1}c^m\rangle - igm\langle\sigma_{22}c^{\dagger m}c^m\rangle$$

$$-ig(2\langle\sigma_{22}c^{\dagger m+1}c^{m+1}\rangle - \langle c^{\dagger m+1}c^{m+1}\rangle)$$

$$-i\sum_{\mathbf{q}}g_{12}^{\mathbf{q}}\langle\sigma_{12}c^{\dagger m+1}c^m(b_{\mathbf{q}}^\dagger + b_{\mathbf{q}})\rangle. \quad (88)$$

In the present objective to study the impact of electron-phonon interaction, the most important contribution is proportional to the phonon- and photon-assisted transition dynamics $\langle\sigma_{12}c^{\dagger m+1}c^m(b_{\mathbf{q}}^\dagger + b_{\mathbf{q}})\rangle$. This transition facilitates photon number-dependent dephasing and blocks the mixing between different photon number manifolds to stabilize the collapse and revival dynamics. The equation of motion read, for example:

$$\frac{\mathrm{d}}{\mathrm{d}t}\langle\sigma_{12}c^{\dagger m+1}c^m b_{\mathbf{q}}^\dagger\rangle = -[(2m+1)\kappa - i\omega_q - i\Delta]\langle\sigma_{12}c^{\dagger m+1}c^m b_{\mathbf{q}}^\dagger\rangle$$

$$-ig_{12}^{\mathbf{q}}\langle b_{\mathbf{q}}^\dagger b_{\mathbf{q}}\rangle\langle\sigma_{12}c^{\dagger m+1}c^m\rangle, \quad (89)$$

where the Born factorization has been applied to second order, neglecting contributions proportional to $\propto gg_{12}^{\mathbf{q}}$. This set of equations of motion corresponds to Section 3.2 for higher-order photon correlations. The set is, however, not closed in terms of the photon number (m). Therefore, depending on the coupling strength g, a sufficient high order in m is taken into account to reach convergence in the calculations. Let us focus on a situation that starts with an inverted QD and a coherent

photon state with a mean photon number $N = 3.5$ [168]. The obtained solution is numerically exact and renders, in the absence of electron–phonon coupling, the well-known Jaynes–Cummings model solutions [28]. Because of the small mean photon number, the collapse and revival phenomenon without acoustical phonons known from the Jaynes–Cummings model [169] is visible only for short times $t < 10$ ps, cf. Figure 16 (orange line in both upper and lower panel). For longer times $t > 15$ ps, the pattern of oscillations becomes irregular and the effect of rephasing vanishes. Excitingly, with phonons for temperatures up to 50 K, the phenomenon is stabilized for much longer times than without phonons (green lines, upper panels for a temperature of 4 K, lower panel for 50 K). The underlying physics is that decoherence manifestly keeps the different photon-assisted Rabi frequencies within the cavity from mixing and allows much longer rephasing dynamics in phase space. This effect

is purely due to the frequency-dependent coupling from the QD to the phonon bath and not included in any Markovian simulations, showing hereby the exciting possibilities provided by non-Markovian, quantum kinetics–induced decoherence. Interestingly, it is even stable against cavity loss but strongly depends on the strong coupling limit between cavity and QD, that is, the cooperativity must be high enough to allow for Rabi oscillations in the microcavity after initialization of the coherent photon field [29, 175]. The experimental challenge lies, however, in the preparation of the initial state, as a perfect coherent superposition initially is essential, however, subjected to losses and transient effect during the preparation stage [168]. These problems have rendered the collapse and revival phenomenon difficult to observe on any platforms. However, if these difficulties can be overcome, QDs with acoustical phonon coupling are ideal candidates to observe long and lasting rephasing, collapse, and revival dynamics, as standard GaAs parameters have been used.
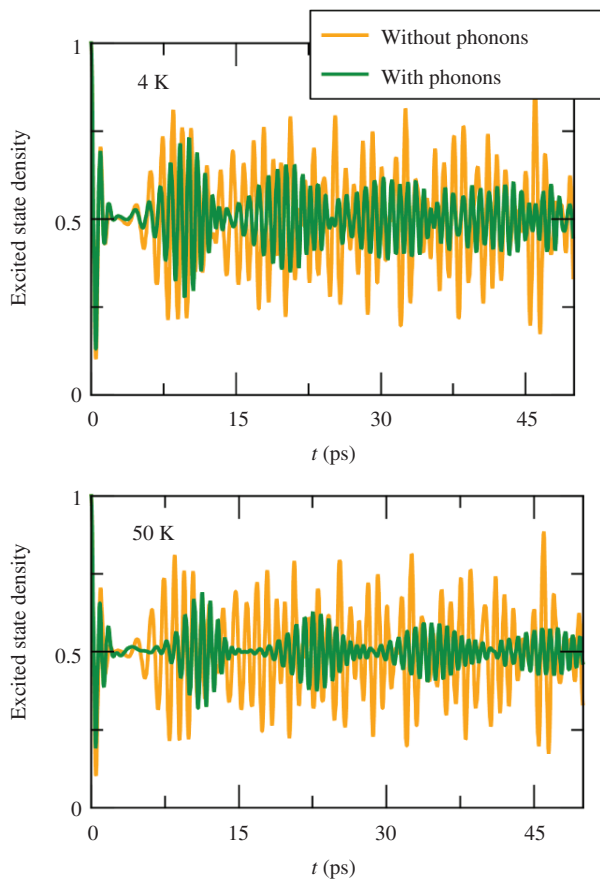
5 Conclusion

In this review, we discussed non-Markovian features in QD-based optical experiments. To understand limits and features of semiconductor nanostructures, it is necessary to unravel the microscopic system–environment dynamics. Electron–phonon interaction is a prominent coupling mechanism, and several examples have been given in which the phonon dynamics cannot be reduced to a Lindblad type of interaction. Phenomenological modeling overestimates typically the dephasing because of the finite memory kernel of phonons, and interesting intrinsical features such as polaron-dressed states and phonon-mediated coherence become inaccessible. Several theoretical models, however, have been presented, which allow to a high-degree of precision to understand quantitatively and qualitatively the physics in semiconductor quantum optics, which in the opinion of the authors have just been started because of advances in experiments and theory to flourish and will continue in doing so. Of particular interest is the investigation of the electron–phonon dynamics beyond the harmonic approximation. As nonequilibrium phonon dynamics is already interesting and partially coherence preserving in the harmonic limit, new effects are to be expected beyond lifetime broadening mechanisms if the electron–phonon interaction is treated beyond second order in its lattice vibrations. Also, detailed investigation on phononic reservoir engineering is on the verge to be realizable in experiments.

Figure 16: The excited state density $\langle \sigma_{22}(t) \rangle$ for a cavity initialized with mean coherent photon number of $N = 3.5$.
The Jaynes–Cummings model solution (orange line) without phonons exhibits only a single collapse with an incomplete revival. Including acoustical phonons (green line) with a lattice temperature of 4 K and 50 K many cycles of collapse and revival are visible.

For example, the impact of acoustic cavities on electronic coherences, phonon lasing, and even on surface-reflected acoustic quantum feedback enables the investigation of exotic light–matter interaction. Because of the high degree of nanotechnological control, collective effects become reachable and superphononance as an acoustic equivalent to superradiance will, maybe, be observed soon. Of fundamental interest is the design of new coupling mechanism and the impact on nonequilibrium steady states and the question arises whether electron–phonon interaction guarantees ergodicity on a microscopical level or not. Here, semiconductor quantum optics may shed light because of nonequilibrium electron–phonon dynamics on the very principles of quantum thermodynamics, heat transport, and possible quantum memory platforms. The fast progress of nanodesign has just begun to address long-standing questions in many-body physics, and, in the belief of the authors, QDs will play their role in this pursuit of understanding fundamental limits of light–matter interaction because of their universal applicability.

References

[1] Michler P, Kiraz A, Becher C, et al. A quantum dot single-photon turnstile device. Science 2000;290:2282–5.

[2] Yuan Z, Kardynal BE, Stevenson RM, et al. Electrically driven single-photon source. Science 2002;295:102–5.

[3] Akopian N, Lindner N, Poem E, et al. Entangled photon pairs from semiconductor quantum dots. Phys Rev Lett 2006;96:130501.

[4] Hafenbrak R, Ulrich S, Michler P, Wang L, Rastelli A, Schmidt O. Triggered polarization-entangled photon pairs from a single quantum dot up to 30 k. New J Phys 2007;9:315.

[5] Santori C, Fattal D, Vučković J, Solomon GS, Yamamoto Y. Indistinguishable photons from a single-photon device. Nature 2002;419:594.

[6] Reithmaier JP, Sek G, Löffler A, et al. Strong coupling in a single quantum dot–semiconductor microcavity system. Nature 2004;432:197.

[7] Woggon U. Optical properties of semiconductor quantum dots. Berlin, Heidelberg, Springer, 1997.

[8] Bimberg D, Grundmann M, Ledentsov NN. Quantum dot heterostructures. Chichester, John Wiley & Sons, 1999.

[9] Kiraz A, Atatüre M, Imamoğlu A. Quantum-dot single-photon sources: prospects for applications in linear optics quantum-information processing. Phys Rev A 2004;69:032305.

[10] Michler P. Single semiconductor quantum dots, vol. 231. Heidelberg, Berlin, Springer, 2009.

[11] Michler P. Quantum dots for quantum information technologies, vol. 237. Berlin, Heidelberg, Springer, 2017.

[12] Jahnke F. Quantum optics with semiconductor nanostructures. Oxford, Woodhead Publishing, 2012.

[13] Rodgers P. Nanoscience and technology. London, UK, Macmillan Publishers Ltd., 2009.

[14] Yu-Ming H, Yu H, Yu-Jia W, et al. On-demand semiconductor single-photon source with near-unity indistinguishability. Nat Nanotechnol 2013;8:213.

[15] Peter E, Hours J, Senellart P, et al. Phonon sidebands in exciton and biexciton emission from single GaAs quantum dots. Phys Rev B 2004;69:041307.

[16] Mendach S, Songmuang R, Kiravittaya S, Rastelli A, Benyoucef M, Schmidt OG. Light emission and wave guiding of quantum dots in a tube. Appl Phys Lett 2006;88:111120.

[17] Schmidt OG. Lateral alignment of epitaxial quantum dots. Heidelberg, Berlin, Springer Science & Business Media, 2007.

[18] Zhang J, Wildmann JS, Ding F, et al. High yield and ultrafast sources of electrically triggered entangledphoton pairs based on strain-tunable quantum dots. Nat Commun 2015;6:10067.

[19] Schlehahn A, Fischbach S, Schmidt R, et al. A stand-alone fiber-coupled single-photon source. Sci Rep 2018;8:1340.

[20] Yoshie T, Scherer A, Hendrickson J, et al. Vacuum rabi splitting with a single quantum dot in a photonic crystal nanocavity. Nature 2004;432:200.

[21] Bose R, Cai T, Choudhury KR, Solomon GS, Waks E. All-optical coherent control of vacuum rabi oscillations. Nat Photonics 2014;8:858–64.

[22] Senellart P, Solomon G, White A. High-performance semiconductor quantum-dot single-photon sources. Nat Nanotechnol 2017;12:1026.

[23] Förstner J, Weber C, Danckwerts J, Knorr A. Phonon-induced damping of rabi oscillations in semiconductor quantum dots. Phys Status Solidi B 2003;238:419–22.

[24] Krummheuer B, Axt VM, Kuhn T, D'Amico I, Rossi F. Pure dephasing and phonon dynamics in GaAs- and GaN-based quantum dot structures: interplay between material parameters and geometry. Phys Rev B 2005;71:235329.

[25] Quilter JH, Brash AJ, Liu F, et al. Phonon-assisted population inversion of a single InGaAs/GaAs quantum dot by pulsed laser excitation. Phys Rev Lett. 2015;114:137401.

[26] Müller M, Bounouar S, Jöns KD, Glässl M, Michler P. On-demand generation of indistinguishable polarization-entangled photon pairs. Nat Photonics 2014;8:224.

[27] Reiter D, Kuhn T, Glässl M, Axt V. The role of phonons for exciton and biexciton generation in an optically driven quantum dot. J Phys Condens Matter 2014;26:423203.

[28] Carmele A, Richter M, Chow WW, Knorr A. Antibunching of thermal radiation by a room-temperature phonon bath: a

numerically solvable model for a strongly interacting light-matter-reservoir system. Phys Rev Lett 2010;104:156801.

[29] Carmele A, Knorr A, Milde F. Stabilization of photon collapse and revival dynamics by a non-markovian phonon bath. New J Phys 2013;15:105024.

[30] Besombes L, Kheng K, Marsal L, Mariette H. Acoustic phonon broadening mechanism in single quantum dot emission. Phys Rev B 2001;63:155307.

[31] Borri P, Langbein W, Schneider S, et al. Ultralong dephasing time in ingaas quantum dots. Phys Rev Lett 2001;87:157401.

[32] Galland C, Högele A, Türeci HE, Imamoğlu A. Non-markovian decoherence of localized nanotube excitons by acoustic phonons. Phys Rev Lett 2008;101:067402.

[33] Vagov A, Croitoru M, Axt VM, Kuhn T, Peeters F. Nonmonotonic field dependence of damping and reappearance of rabi oscillations in quantum dots. Phys Rev Lett 2007;98:227403.

[34] Madsen KH, Ates S, Lund-Hansen T, et al. Observation of non-markovian dynamics of a single quantum dot in a micropillar cavity. Phys Rev Lett 2011;106:233601.

[35] Carmichael HJ. Statistical methods in quantum optics 1. Berlin, Heidelberg, Springer Science & Business Media, 2009.

[36] Scully MO, Zubairy MS. Quantum optics. Am J Phys 1999;67:648.

[37] Breuer H-P, Petruccione F. The theory of open quantum systems. Oxford, Oxford University Press, 2002.

[38] Gardiner C, Zoller P, Zoller P. Quantum noise: a handbook of markovian and non- markovian quantum stochastic methods with applications to quantum optics, vol. 56. Berlin, Heidelberg, Springer Science & Business Media, 2004.

[39] Breuer H-P, Laine E-M, Piilo J, Vacchini B. Colloquium: non-markovian dynamics in open quantum systems. Rev Mod Phys 2016;88:021002.

[40] Cerrillo J, Cao J. Non-markovian dynamical maps: numerical processing of open quantum trajectories. Phys Rev Lett 2014;112:110401.

[41] de Vega I, Alonso D. Dynamics of non-markovian open quantum systems. Rev Mod Phys 2017;89:015001.

[42] Michler P. Single quantum dots: fundamentals, applications and new concepts, vol. 90. Berlin, Heidelberg, Springer Science & Business Media, 2003.

[43] Stock E, Dachner M-R, Warming T, et al. Acoustic and optical phonon scattering in a single In(Ga)As quantum Dot. Phys Rev B 2011;83:041304.

[44] Strauß M, Carmele A, Schneider J, et al. Wigner time delay induced by a single quantum dot. Phys Rev Lett 2019;122:107401.

[45] Ramsay A, Godden T, Boyle S, et al. Phonon-induced rabi-frequency renormalization of optically driven single InGaAs/GaAs quantum dots. Phys Rev Lett 2010;105:177402.

[46] Kaldewey T, Lüker S, Kuhlmann AV, et al. Demonstrating the decoupling regime of the electron-phonon interaction in a quantum dot using chirped optical excitation. Phys Rev B 2017;95:241306.

[47] Bounouar S, Müller M, Barth A, Glässl M, Axt V, Michler P. Phonon-assisted robust and deterministic two-photon biexciton preparation in a quantum dot. Phys Rev B 2015;91:161302.

[48] Ardelt P-L, Hanschke L, Fischer KA, et al. Dissipative preparation of the exciton and biexciton in self-assembled quantum dots on picosecond time scales. Phys Rev B 2014;90:241404.

[49] Iles-Smith J, Nazir A. Quantum correlations of light and matter through environmental transitions. Optica 2016;3:207–11.

[50] Weiler S, Ulhaq A, Ulrich SM, et al. Phonon-assisted incoherent excitation of a quantum dot and its emission properties. Phys Rev B 2012;86:241304.

[51] Hohenester U. Cavity quantum electrodynamics with semiconductor quantum dots: role of phonon-assisted cavity feeding. Phys Rev B 2010;81:155303.

[52] Monniello L, Tonin C, Hostein R, et al. Excitation-induced dephasing in a resonantly driven InAs/GaAs quantum dot. Phys Rev Lett 2013;111:026403.

[53] Ulrich S, Ates S, Reitzenstein S, Löffler A, Forchel A, Michler P. Dephasing of triplet-sideband optical emission of a resonantly driven InAs/GaAs quantum dot inside a microcavity. Phys Rev Lett 2011;106:247402.

[54] Roy C, Hughes S. Phonon-dressed mollow triplet in the regime of cavity quantum electrodynamics: excitation-induced dephasing and nonperturbative cavity feeding effects. Phys Rev Lett 2011;106:247403.

[55] Gardiner C, Zoller P. Quantum noise. Berlin Heidelberg New York, Springer, 1991.

[56] Bányai L, Koch SW. Semiconductor quantum dots, vol. 2. Singapore, River Edge, NJ, World Scientific, 1993.

[57] Grundmann M, Stier O, Bimberg D. InAs/GaAs pyramidal quantum dots: strain distribution, optical phonons, and electronic structure. Phys Rev B 1995;52:11969–81.

[58] Stier O, Grundmann M, Bimberg D. Electronic and optical properties of strained quantum dots modeled by 8-band k · p theory. Phys Rev B 1999;59:5688–701.

[59] Schliwa A, Winkelnkemper M, Bimberg D. Impact of size, shape, and composition on piezoelectric effects and electronic properties of In(Ga)As\GaAs quantum dots. Phys Rev B 2007;76:205324.

[60] Chow WW, Jahnke F. On the physics of semiconductor quantum dots for applications in lasers and quantum optics. Prog. Quant Electron 2013;37:109–84.

[61] Haug H Koch SW. Quantum theory of the optical and electronic properties of semiconductors, 5th ed. Singapore, World Scientific Publishing Company, 2009.

[62] Brandes T. Coherent and collective quantum optical effects in mesoscopic systems. Phys Rep 2005;408:315.

[63] Sakaki H. Quantum wires, quantum boxes and related structures: physics, device potentials and structural requirements. Surf Sci 1992;267:623–9.

[64] Schwab K, Henriksen E, Worlock J, Roukes ML. Measurement of the quantum of thermal conductance. Nature 2000;404:974.

[65] Gornyi I, Mirlin A, Polyakov D. Interacting electrons in disordered wires: Anderson localization and low-T transport. Phys Rev Lett 2005;95:206603.

[66] Sun C-K, Liang J-C, Yu X-Y. Coherent acoustic phonon oscillations in semiconductor multiple quantum wells with piezoelectric fields. Phys Rev Lett 2000;84:179.

[67] Lugli P, Goodnick S. Nonequilibrium longitudinal-optical phonon effects in GaAs-AlGaAs quantum wells. Phys Rev Lett 1987;59:716.

[68] Kim D-S, Shah J, Cunningham J, et al. Giant excitonic resonance in time-resolved four-wave mixing in quantum wells. Phys Rev Lett 1992;68:1006.

[69] Gammon D, Rudin S, Reinecke T, Katzer D, Kyono C. Phonon broadening of excitons in GaAs/Al x Ga 1- x As quantum wells. Phys Rev B 1995;51:16785.

[70] Richter M, Singh R, Siemens M, Cundiff ST. Deconvolution of optical multidimensional coherent spectra. Sci. Adv. 2018;4:eaar7697.

[71] Singh R, Richter M, Moody G, Siemens ME, Li H, Cundiff ST. Localization dynamics of excitons in disordered semiconductor quantum wells. Phys Rev B 2017;95:235307.

[72] Lim J, Ing DJ, Rosskopf J, et al. Signatures of spatially correlated noise and non-secular effects in two-dimensional electronic spectroscopy. J Chem Phys 2017;146:024109.

[73] Wigger D, Schneider C, Gerhardt S, et al. Rabi oscillations of a quantum dot exciton coupled to acoustic phonons: coherence and population readout. Optica 2018;5:1442–50.

[74] Cassette E, Pensack RD, Mahler B, Scholes GD. Room-temperature exciton coherence and dephasing in two-dimensional nanostructures. Nat Commun 2015;6:6086.

[75] Liu A, Almeida DB, Bae WK, Padilha LA, Cundiff ST. Vibrational coupling modifies spectral diffusion in core-shell colloidal quantum dots. arXiv preprint arXiv:1806.06112, 2018.

[76] Suzuki T, Singh R, Moody G, et al. Dephasing of InAs quantum dot p-shell excitons studied using two-dimensional coherent spectroscopy. Phys Rev B 2018;98:195304.

[77] Christiansen D, Selig M, Berghäuser G, et al. Phonon sidebands in monolayer transition metal dichalcogenides. Phys Rev Lett 2017;119:187402.

[78] Malic E, Knorr A. Graphene and carbon nanotubes: ultrafast optics and relaxation dynamics. Weinheim, John Wiley & Sons, 2013.

[79] Kira M, Koch SW. Semiconductor quantum optics. Cambridge, Cambridge University Press, 2011.

[80] Hohenester U, Laucht A, Kaniber M, et al. Phonon-assisted transitions from quantum dot excitons to cavity photons. Phys Rev B 2009;80:201311.

[81] Briegel H-J, Dür W, Cirac JI, Zoller P. Quantum repeaters: the role of imperfect local operations in quantum communication. Phys Rev Lett 1998;81:5932–5.

[82] Kimble HJ. The quantum internet. Nature 2008;453:1023.

[83] Mukamel S. Principles of nonlinear optical spectroscopy, vol. 29. New York, Oxford University Press, 1995.

[84] Axt VM, Mukamel S. Nonlinear optics of semiconductor and molecular nanostructures; a common perspective. Rev Mod Phys 1998;70:145–74.

[85] Warburton RJ. Single spins in self-assembled quantum dots. Nat Mater 2013;12:483.

[86] Matthiesen C, Vamivakas AN, Atatüre M. Subnatural linewidth single photons from a quantum dot. Phys Rev Lett 2012;108:093602.

[87] May V, Kühn O. Charge and energy transfer dynamics in molecular systems. Weinheim, John Wiley & Sons, 2008.

[88] Bourgain R, Pellegrino J, Jennewein S, et al. Direct measurement of the wigner time delay for the scattering of light by a single atom. Opt Lett 2013;38:1963–5.

[89] Sondermann M, Leuchs G. The phase shift induced by a single atom in free space. J Eur Opt Soc – Rapid 2013;8. DOI: 10.2971/jeos.2013.13052.

[90] Palatchi C, Dahlstrm JM, Kheifets AS, et al. Atomic delay in helium, neon, argon and krypton. J Phys B At Mol Opt Phys 2014;47:245003.

[91] Kira M, Koch S. Many-body correlations and excitonic effects in semiconductor Spectroscopy. Prog Quantum Electron 2006;30:155–296.

[92] Čížek J. On the use of the cluster expansion and the technique of diagrams in calculations of correlation effects in atoms and molecules. In: LeFebvre R, Moser C, eds. Advances in Chemical Physics. Hoboken, NJ, USA, John Wiley & Sons, Ltd., 1969, 35–89.

[93] Krummheuer B, Axt VM, Kuhn T. Theory of pure dephasing and the resulting absorption line shape in semiconductor quantum dots. Phys Rev B 2002;65:195313.

[94] Richter M, Carmele A, Sitek A, Knorr A. Few-photon model of the optical emission of semiconductor quantum dots. Phys Rev Lett 2009;103:087407.

[95] Rozbicki E, Machnikowski P. Quantum kinetic theory of pho-non-assisted excitation transfer in quantum dot molecules. Phys Rev Lett 2008;100:027401.

[96] Lüker S, Kuhn T, Reiter DE. Phonon impact on optical control schemes of quantum dots: role of quantum dot geometry and symmetry. Phys Rev B 2017;96:245306.

[97] Wilson-Rae I, Imamoğlu A. Quantum dot cavity-qed in the presence of strong electron-phonon interactions. Phys Rev B 2002;65:235311.

[98] Laussy F, Valle ED, Mnchen T, et al. 9 – Luminescence spectra of quantum dots in microcavities. In: Jahnke F, ed. Quantum Optics with Semiconductor. Oxford, Woodhead Publishing, 2012, 293–331.

[99] Laussy FP, Laucht A, del Valle E, Finley JJ, Villas-Bôas JM. Luminescence spectra of quantum dots in microcavities. III. Multiple quantum dots. Phys Rev B 2011;84:195313.

[100] del Valle E. Microcavity quantum electrodynamics. Saarbrcken, VDM Verlag, 2010.

[101] del Valle E, Laussy FP. Mollow triplet under incoherent pumping. Phys Rev Lett 2010;105:233601.

[102] Kreinberg S, Grběsić T, Strauß M, et al. Quantum-optical spectroscopy of a two-level system using an electrically driven micropillar laser as a resonant excitation source. Light Sci Appl 2018;7:Article number: 41.

[103] McCutcheon DPS, Dattani NS, Gauger EM, Lovett BW, Nazir A. Quantum dot rabi rotations beyond the weak exciton-phonon coupling regime. Phys Rev B 2011;84:081305.

[104] Manson R, Roy-Choudhury K, Hughes S. Polaron master equation theory of pulse-driven phonon-assisted population inversion and single-photon emission from quantum-dot excitons. Phys Rev B 2016;93:155423.

[105] Kabuss J, Carmele A, Richter M, Chow WW, Knorr A. Inductive equation of motion approach for a semiconductor qd-qed: Coherence induced control of photon statistics. Phys Status Sol B 2011;248:872–8.

[106] Axt V, Herbst M, Kuhn T. Coherent control of phonon quantum beats. Superlattices Microstruct 1999;26:117–28.

[107] Kabuss J, Carmele A, Richter M, Knorr A. Microscopic equation-of-motion approach to the multiphonon assisted quantum emission of a semiconductor quantum dot. Phys Rev B 2011;84:125324.

[108] Glässl M, Vagov A, Lüker S, et al. Long-time dynamics and stationary nonequilibrium of an optically driven strongly confined quantum dot coupled to phonons. Phys Rev B 2011;84:195311.

[109] Schollwöck U. The density-matrix renormalization group in the age of matrix product states. Ann Phys 2011;326:96–192.

[110] Caldeira AO, Leggett AJ. Path integral approach to quantum brownian motion. Phys A Stat Mech Appl 1983;121:587–616.

[111] Vidal G. Phys Rev Lett 2004;93:040502.

[112] del Pino J, Schröder FAYN, Chin AW, Feist J, Garcia-Vidal FJ. Tensor network simulation of non-markovian dynamics in organic polaritons. Phys Rev Lett 2018;121:227401.

[113] Strathearn A, Kirton P, Kilda D, Keeling J, Lovett BW. Efficient non-markovian quantum dynamics using time-evolving matrix product operators. Nat Commun 2018;9:3322.

[114] Droenner L, Naumann NL, Schöll E, Knorr A, Carmele A. Quantum Pyragas control: selective control of individual photon probabilities. Phys Rev A 2019;99:023840.

[115] Makri N. Quantum dissipative dynamics: a numerically exact methodology. J Phys Chem A 1998;102:4414–27.

[116] Cygorek M, Barth AM, Ungar F, Vagov A, Axt VM. Nonlinear cavity feeding and unconventional photon statistics in solid-state cavity qed revealed by many-level real-time path-integral calculations. Phys Rev B 2017;96:201201.

[117] Hopfmann C, Musiał A, Strauß M, et al. Compensation of phonon-induced renormalization of vacuum rabi splitting in large quantum dots: towards temperature-stable strong coupling in the solid state with quantum dot-micropillars. Phys Rev B 2015;92:245403.

[118] Jackson JD. Classical electrodynamics. New York, John Wiley & Sons, 2012.

[119] Allen L, Eberly JH. Optical resonance and two-level atoms, vol. 28. New York, Dover Publication, Courier Corporation, 1987.

[120] Gardiner C. Stochastic methods, vol. 4. Berlin, Springer, 2009.

[121] Jakubczyk T, Delmonte V, Fischbach S, et al. ACS Photonics 2016;3:2461–6.

[122] Fras F, Mermillod Q, Nogues G, et al. Impact of phonons on dephasing of individual excitons in deterministic quantum dot microlenses. Nat Photonics 2016;10:155.

[123] Madelung O. Introduction to solid-state theory, vol. 2. Berlin, Heidelberg, Springer Science & Business Media, 2012.

[124] Pullerits T, Monshouwer R, van Mourik F, van Grondelle R. Temperature dependence of electron-vibronic spectra of photosynthetic systems. Computer simulations and comparison with experiment. Chem Phys 1995;194:395–407.

[125] Cohen-Tannoudji C, Guéry-Odelin D. Advances in atomic physics: an overview. Singapore, World Scientific Publishing Co. Pte. Ltd., 2011.

[126] Gardiner C, Zoller P. The quantum world of ultra-cold atoms and light book II: the physics of quantum-optical devices. Singapore, World Scientific, 2015, 1–524.

[127] McCutcheon DP, Nazir A. Quantum dot rabi rotations beyond the weak exciton–phonon coupling regime. New J Phys 2010;12:113042.

[128] Kabuss J, Werner S, Hoffmann A, Hildebrandt P, Knorr A, Richter M. Theory of time-resolved raman scattering and fluorescence emission from semiconductor quantum dots. Phys Rev B 2010;81:075314.

[129] Carmele A, Knorr A, Richter M. Photon statistics as a probe for exciton correlations in coupled nanostructures. Phys Rev B 2009;79:035316.

[130] Ramsay AJ, Gopal AV, Gauger EM, et al. Damping of exciton rabi rotations by acoustic phonons in optically excited InGaAs/GaAs quantum dots. Phys Rev Lett 2010;104:017402.

[131] Glässl M, Croitoru MD, Vagov A, Axt VM, Kuhn T. Influence of the pulse shape and the dot size on the decay and reappearance of rabi rotations in laser driven quantum dots. Phys Rev B 2011;84:125304.

[132] Machnikowski P, Jacak L. Resonant nature of phonon-induced damping of rabi oscillations in quantum dots. Phys Rev B 2004;69:193302.

[133] Krügel A, Axt VM, Kuhn T. Transition from jaynes-cummings to autler-townes ladder in a quantum dot–microcavity system. Phys Rev B 2006;73:035302.

[134] Reiter DE. Time-resolved pump-probe signals of a continuously driven quantum dot affected by phonons. Phys Rev B 2017;95:125308.

[135] Naumann NL, Droenner L, Chow WW, Kabuss J, Carmele A. Solid-state-based analog of optomechanics. JOSA B 2016;33:1492–501.

[136] Droenner L, Naumann NL, Kabuss J, Carmele A. Collective enhancements in many-emitter phonon lasing. Phys Rev A 2017;96:043805.

[137] Kabuss J, Carmele A, Brandes T, Knorr A. Optically driven quantum dots as source of coherent cavity phonons: a proposal for a phonon laser scheme. Phys Rev Lett 2012;109:054301.

[138] Kepesidis KV, Bennett SD, Portolan S, Lukin MD, Rabl P. Phonon cooling and lasing with nitrogen-vacancy centers in diamond. Phys Rev B 2013;88:064105.

[139] Czerniuk T, Wigger D, Akimov AV, et al. Picosecond control of quantum dot laser emission by coherent phonons. Phys Rev Lett 2017;118:133901.

[140] Richter M, Knorr A. A time convolution less density matrix approach to the nonlinear optical response of a coupled system–bath complex. Ann Phys 2010;325:711–47.

[141] Stauber T, Zimmermann R, Castella H. Electron-phonon interaction in quantum dots: a solvable model. Phys Rev B 2000;62:7336–43.

[142] Heitz R, Mukhametzhanov I, Stier O, Madhukar A, Bimberg D. Enhanced polar exciton-lo-phonon interaction in quantum dots. Phys Rev Lett 1999;83:4654–7.

[143] Heitz R, Born H, Guffarth F, et al. Existence of a phonon bottleneck for excitons in quantum dots. Phys. Rev. B 2001;64:241305.

[144] Droenner L, Finsterhölzl R, Heyl M, Carmele A. Stabilizing a discrete time crystal against dissipation. arXiv preprint arXiv:1902.04986, 2019.

[145] Leggett AJ, Chakravarty S, Dorsey AT, Fisher MPA, Garg A, Zwerger W. Dynamics of the dissipative two-state system. Rev Mod Phys 1987;59:1.

[146] Vagov A, Croitoru M, Axt V, Kuhn T, Peeters F. High pulse area undamping of rabi oscillations in quantum dots coupled to phonons. Phys Status Sol B 2006;243:2233–40.

[147] Vagov A, Croitoru M, Axt V, Machnikowski P, Kuhn T. Dynamics of quantum dots with strong electron phonon coupling: Correlation expansion vs. path integrals. Phys Status Sol B 2011;248:839–42.

[148] Dousse A, Lanco L, Suffczyński J, et al. Controlled light-matter coupling for a single quantum dot embedded in a pillar microcavity using far-field optical lithography. Phys Rev Lett 2008;101:267404.

[149] Gschrey M, Gericke F, Schüßler A, et al. In situ electron-beam lithography of deterministic single-quantum-dot mesa-structures using low-temperature cathodoluminescence spectroscopy. Appl Phys Lett 2013;102:251113.

[150] Sotier F, Thomay T, Hanke T, et al. Femtosecond few-fermion dynamics and deterministic single-photon gain in a quantum dot. Nat Phys 2009;5:352.

[151] Flagg EB, Muller A, Robertson J, et al. Resonantly driven coherent oscillations in a solid-state quantum emitter. Nat Phys 2009;5:203.

[152] Laussy FP, Del Valle E, Tejedor C. Strong coupling of quantum dots in microcavities. Phys Rev Lett 2008;101:083601.

[153] Kasprzak J, Reitzenstein S, Muljarov EA, et al. Up on the jaynes–cummings ladder of a quantum-dot/microcavity system. Nat Mater 2010;9:304.

[154] Kavokin A. Microcavities, 21. New York, Oxford University Press Inc., 2017.

[155] Lodahl P, Mahmoodian S, Stobbe S. Interfacing single photons and single quantum dots with photonic nanostructures. Rev Mod Phys 2015;87:347–400.

[156] Schneebeli L, Kira M, Koch SW. Characterization of strong light-matter coupling in semiconductor quantum-dot microcavities via photon-statistics spectroscopy. Phys Rev Lett 2008;101:097401.

[157] Hopfmann C, Carmele A, Musiał, et al. Transition from jaynes-cummings to autler-townes ladder in a quantum dot–microcavity system. Phys. Rev. B 2017;95:035302.

[158] Lounis B, Orrit M. Single-photon sources. Rep Prog Phys 2005;68:1129.

[159] Ding X, He Y, Duan Z-C, et al. On-demand single photons with high extraction efficiency and near-unity indistinguishability from a resonantly driven quantum dot in a micropillar. Phys Rev Lett 2016;116:020401.

[160] Somaschi N, Giesz V, De Santis L, et al. Near-optimal single-photon sources in the solid state. Nat Photonics 2016;10:340.

[161] Iles-Smith J, McCutcheon DP, Nazir A, Mørk J. Phonon scattering inhibits simultaneous near-unity efficiency and indistinguishability in semiconductor single-photon sources. Nat Photonics 2017;11:521.

[162] Calic M, Gallo P, Felici M, et al. Phonon-mediated coupling of InGaAs/GaAs quantum-dot excitons to photonic crystal cavities. Phys Rev Lett 2011;106:227402.

[163] Kaer P, Nielsen TR, Lodahl P, Jauho A-P, Mørk J. Non-markovian model of photon-assisted dephasing by electron-phonon interactions in a coupled quantum-dot–cavity system. Phys Rev Lett 2010;104:157401.

[164] Hughes S, Yao P, Milde F, et al. Influence of electron-acoustic phonon scattering on off-resonant cavity feeding within a strongly coupled quantum-dot-cavity system. Phys Rev B 2011;83:165313.

[165] Winger M, Volz T, Tarel G, et al. Explanation of photon correlations in the far-off-resonance optical emission from a quantum-dot–cavity system. Phys Rev Lett 2009;103:207403.

[166] Carmele A, Kabuss J, Chow WW. Highly detuned rabi oscillations for a quantum dot in a microcavity. Phys Rev B 2013;87:041305.

[167] Thoma A, Schnauber P, Gschrey M, et al. Exploring dephasing of a solid-state quantum emitter via time- and temperature-dependent hong-ou-mandel experiments. Phys Rev Lett 2016;116:033601.

[168] Rempe G, Walther H, Klein N. Observation of quantum collapse and revival in a one-atom maser. Phys Rev Lett 1987;58:353–6.

[169] Eberly JH, Narozhny NB, Sanchez-Mondragon JJ. Periodic spontaneous collapse and revival in a simple quantum model. Phys Rev Lett 1980;44:1323–6.

[170] Hong CK, Ou ZY, Mandel L. Measurement of subpicosecond time intervals between two photons by interference. Phys Rev Lett 1987;59:2044–6.

[171] Galperin YM, Altshuler BL, Bergli J, Shantsev DV. Non-gaussian low-frequency noise as a source of qubit decoherence. Phys Rev Lett 2006;96:097009.

[172] Laikhtman BD. General theory of spectral diffusion and echo decay in glasses. Phys Rev B 1985;31:490–504.

[173] Eberly JH, Wódkiewicz K, Shore BW. Noise in strong laser-atom interactions: phase telegraph noise. Phys Rev A 1984;30:2381–9.

[174] Liu J, Konthasinghe K, Davanço M, et al. Single self-assembled InAs/GaAs quantum dots in photonic nanostructures: the role of nanofabrication. Phys Rev Appl 2018;9:064019.

[175] Glässl M, Sörgel L, Vagov A, Croitoru MD, Kuhn T, Axt VM. Interaction of a quantum-dot cavity system with acoustic phonons: Stronger light-matter coupling can reduce the visibility of strong coupling effects. Phys Rev B 2012;86:035319.